Multiqubit gate based on parity cross resonance

Xuexin Xu,[1,2,*] Siyu Wang,[1,3] Radhika Joshi,[1,3] Rihan Hai,[4] and Mohammad H. Ansari[1,2]

[1] *Peter Grünberg Institute, Forschungszentrum Jülich, Jülich 52425, Germany*

[2] *Jülich-Aachen Research Alliance (JARA), Fundamentals of Future Information Technologies, Jülich 52425, Germany*

[3] *Institute for Quantum Information, RWTH Aachen University, D-52056 Aachen, Germany*

[4] *Department of Software Technology, Delft University of Technology, Delft, Netherlands*

(Received 11 November 2025; revised 23 January 2026; accepted 17 March 2026; published 17 April 2026)

The realization of multiqubit entangling gates is essential for efficient, scalable, and fault-tolerant quantum information processing, reducing algorithmic complexity and circuit depth. We demonstrate a native three-qubit entangling gate implemented by simultaneously driving all qubits at a common frequency, exploiting engineered interactions to realize multicontrol operations in a single coherent step. By optimizing the conditional dynamics originating from drive-induced nonlocal contamination, desired interaction channels are selectively enhanced while spurious terms are suppressed, ensuring robust performance within the computational subspace. This gate enables key applications, including deterministic GHZ-state generation, Toffoli-class logic with a shortest gate duration of 90 ns and a highest fidelity of 99.72%, and a controlled-*ZZ* gate tailored for fast surface-code quantum error correction. Simulations based on realistic IBM device parameters indicate that the gate maintains high fidelity and resilience under increasing excitation numbers and larger Hilbert-space dimensions. Our results establish a foundation for co-designing circuit architectures and control strategies that harness native multiqubit interactions as fundamental building blocks for next-generation superconducting quantum processors, thereby enabling improved gate performance with more flexible tuning of circuit parameters.

DOI: 10.1103/6d5v-vrm4

I. INTRODUCTION

Multiqubit entangling gates are essential for enhancing the efficiency and scalability of quantum information processing. Instead of decomposing multiqubit operations into lengthy sequences of two-qubit gates [1–3], higher-order entangling gates can directly generate complex correlations, such as Greenberger-Horne-Zeilinger (GHZ) states or the *i*Toffoli gate, in a single step. These native multiqubit interactions offer a compact representation of nonlocal transformations and enable more efficient implementations of quantum error-correcting codes, variational ansätze, and many-body simulations. Exploiting intrinsic multibody couplings in platforms such as trapped ions [4–7], Rydberg atoms [8–11], or superconducting circuits [12–15] further improves fidelity and execution time, making the control of genuine multiqubit entanglement a key milestone toward large-scale, fault-tolerant quantum computation.

Multipartite entangled states, such as GHZ, *W*, and Dicke states, serve as fundamental resources for a wide range of quantum information protocols, including quantum teleportation, superdense coding, and measurement-based quantum computation. The capability to efficiently generate, manipulate, and preserve such entanglement is therefore essential for achieving scalable and fault-tolerant quantum technologies. Recent experimental progress includes the generation of a 10-qubit *W* state with a fidelity of 91.3% and a double-excitation Dicke state with a fidelity of 92.6% [16], as well as the reported largest 120-qubit GHZ state with a fidelity of 56% demonstrated on IBM quantum processors [17].

Direct multiqubit gates can substantially reduce circuit depth, thereby mitigating cumulative errors, minimizing decoherence, and enhancing computational efficiency. One approach is to synchronize interactions, for example, aligning spin-orbit coupling and orbital magnetic fields to realize a $C^2R_y(\pi)$ gate on spin-qubit platforms [18]. Another practical route is through simultaneous two-qubit operations, such as the controlled-controlled-*Z* and controlled-*i*SWAP gates, realized via parallel two-qubit operations on

*Contact author: x.xu@fz-juelich.de

different qubit pairs [19–21] on superconducting circuits, as well as the one-step three-qubit parity gate [22] and the *i*Toffoli gate [12], implemented via concurrent cross-resonance (CR) microwave drives applied to all qubits [23–28]. Typically, these multiqubit gates would require at least six two-qubit CNOT-like operations if decomposed sequentially; leveraging the simultaneous-gate approach markedly reduces gate count and execution time, thereby improving overall circuit robustness and efficiency.

However, simultaneous-gate approaches trade off unwanted parasitic couplings to enable the joint implementation of multiple gates, limiting achievable fidelities and demanding careful circuit optimization. To overcome these challenges, we develop and benchmark a general protocol for synthesizing a single-shot parity cross-resonance (PCR) gate characterized by a direct three-qubit *ZZX* interaction in fixed-frequency transmon circuits [29]. In contrast to Refs. [12,22], which rely on simultaneous two-qubit interactions, this method combines perturbative design with gradient-free, nonperturbative optimization to realize a one-step three-body interaction beyond the dispersive regime, while automatically identifying optimal static operating parameters and suppressing stray interactions. Applied to a representative three-qubit layout based on IBM parameters, the protocol identifies broad operating regions supporting strong *ZX*-like rates, enabling high-fidelity GHZ-state preparation and single-shot CCNOT and *i*Toffoli gate implementations. It also extends naturally to quantum error correction by adapting the controlled-*ZZ* (CZZ) gate for direct parity mapping, enhancing both speed and fidelity.

The paper is organized as follows: In Sec. II, we outline the principles of the three-body interaction quantum logic gate and its applications to GHZ state preparation (Sec. II A 1), CCNOT-like implementation (Sec. II A 2), and error-correction-oriented controlled-*ZZ* gates (Sec. II A 3), followed by their individual implementations (Sec. II B). In Sec. III, we describe our gradient-free optimization framework for modeling and tuning the gate parameters. Finally, Sec. IV presents performance validation for the three main examples: GHZ triplet state (Sec. IV A), CCNOT-like gate (Sec. IV B), and CZZ gate (Sec. IV C).

II. PRINCIPLE

The *ZZX* interaction, typically arising as a higher-order by-product of two simultaneous CR gates, is often neglected in standard gate synthesis procedures. Yet, under specific operating conditions—detailed later in the paper—this three-body term can be significantly amplified. When acting on three qubits with all-to-all connectivity, the *ZZX* interaction implements a *Z*-parity check between the first two qubits while simultaneously flipping the state of the third. This flexibility makes the *ZZX* interaction a valuable fundamental building block for quantum error detection schemes [20], and leads us to introduce it as the *parity cross-resonance* (PCR) gate.

Native multiqubit interactions constitute a foundational asset in quantum logic synthesis, as they permit the direct implementation of otherwise composite operations—operations that, in their conventional form, require sequences of two-qubit gates interspersed with single-qubit rotations. Harnessing such intrinsic couplings not only compresses circuit depth but also suppresses spurious Hamiltonian terms, thereby improving both the fidelity and resilience of entanglement generation on noisy intermediate-scale quantum (NISQ)-era superconducting platforms. Inspired by these benefits, we now proceed to investigate how the PCR gate can be leveraged to streamline quantum circuit design and to realize efficient, hardware-native multiqubit operations.

A. Quantum logic

We now present practical protocols that exploit the $U_{ZZX}(\theta)$ interaction to enable efficient entanglement generation via the PCR gate. The associated unitary action on computational basis states $|q_1q_2q_3\rangle$ $(q_1, q_2, q_3 \in \{0, 1\})$ is given by

$$U_{ZZX}(\theta)\,|q_1q_2q_3\rangle = \cos\left(\frac{\theta}{2}\right)|q_1q_2q_3\rangle - i(-1)^{q_1\oplus q_2}\sin\left(\frac{\theta}{2}\right)|q_1q_2\overline{q_3}\rangle\,. \quad (1)$$

For the case of π rotation, the operator returns the following values:

$$U_{ZZX}(\pi)\,|q_1q_2q_3\rangle = \begin{cases} -i\,|q_1q_2\overline{q_3}\rangle & \text{if } q_1 = q_2 \\ +i\,|q_1q_2\overline{q_3}\rangle & \text{if } q_1 = \overline{q_2} \end{cases}.$$

A 2π rotation returns the state back on itself, which indicates that by negating the rotation angle $\pi \to -\pi$ the gate is inverted. Moreover, the gate at $\pi/2$ rotation creates a conditional superposition on the third qubit:

$$U_{ZZX}\left(\frac{\pi}{2}\right)|q_1q_2q_3\rangle = \begin{cases} \frac{1}{\sqrt{2}}\,|q_1q_2\rangle\,(|q_3\rangle - i\,|\overline{q_3}\rangle) & \text{if } q_1 = q_2 \\ \frac{1}{\sqrt{2}}\,|q_1q_2\rangle\,(|q_3\rangle + i\,|\overline{q_3}\rangle) & \text{if } q_1 = \overline{q_2} \end{cases}.$$

These capabilities are particularly valuable for three key purposes: (1) the preparation of Greenberger-Horne-Zeilinger (GHZ) entangled states, and (2) the implementation of a CCNOT-like multiqubit gate, (3) the realization of controlled-*ZZ* (CZZ) gate.

1. GHZ state preparation

A GHZ state is a maximally entangled multiqubit state of the form $|\mathrm{GHZ}\rangle = \frac{1}{\sqrt{2}}(|000\cdots\rangle + |111\cdots\rangle)$. Such states serve as fundamental resources in quantum information processing [30], playing critical roles in nonlocality tests [31], quantum error correction [32,33], and entanglement-based protocols [34,35]. Mitigating errors during GHZ state preparation involves reducing the effects of decoherence, gate imperfections, and crosstalk encountered during entangling operations. Recent advancements include the use of quantum autoencoders, which are trained to compress and reconstruct entangled input states, offering a data-driven approach to error mitigation [36].

Since the ZZX interaction can be regarded as a three-qubit analog of the two-qubit ZX gate, we begin by recalling the preparation of a Bell state using the CR mechanism. Bell states constitute a subset of maximally entangled two-qubit states and admit natural generalizations to multipartite settings, such as GHZ states. The two-qubit Z_1X_2 interaction of CR gate enables the creation of the maximally entangled Bell state via the following gate sequence: $S_2H_1U_{Z_1X_2}(\pi/2)H_1\,|00\rangle = (|00\rangle + |11\rangle)/\sqrt{2}$, where S_i and H_i represent the phase and Hadamard gate, respectively, acting on qubit i, and the U_{ZX} rotation is defined as $U_{Z_1X_2}(\theta) = \cos(\theta/2)\,I_1I_2 - i\sin(\theta/2)\,Z_1X_2$.

By analogy with the two-qubit CR gate, the three-qubit ZZX interaction can be harnessed to directly generate a GHZ state. In particular, we consider the following protocol. $S_3H_2H_1U_{Z_1Z_2X_3}(\pi/2)H_1H_2\,|000\rangle = (|000\rangle + |111\rangle)/\sqrt{2}$. Here, the central operation—$U_{Z_1Z_2X_3}(\pi/2)$—corresponds to evolution under the ZZX Hamiltonian for a time corresponding to a $\pi/2$ rotation. The gate sequence $H_iZ_iH_i$ transforms the Z_i operator into X_i, and the inclusion of the phase gate S_i compensates for the acquired phase. This composite circuit consists of five single-qubit gates (typically ultrafast and high-fidelity) in conjunction with a single three-qubit entangling gate. The resulting operation effectively realizes an interaction $U_{XXX}(\pi/2)$, which entangles all three qubits and maps the initial product state $|000\rangle$ to a GHZ state. This construction highlights the utility of native three-body interactions in reducing circuit complexity. Compared to the conventional GHZ state preparation protocol—typically requiring two CNOT gates—the ZZX-based protocol provides a compact alternative by replacing both entangling gates with a *single* three-qubit unitary. The prerequisite for this replacement is that the three-qubit gate is applied in one go on three all-in-all interacting qubits, thus the chain structure is not favorable.

2. A three-qubit CCNOT

Another natural application of the PCR gate is the implementation of multiqubit logic gates. In particular, the three-qubit Toffoli gate—also known as the CCNOT gate—plays a central role in quantum information processing. As a universal gate for reversible classical computation, it enables the realization of arbitrary Boolean functions on quantum registers [37]. Conventional synthesis of Toffoli-like gates typically requires at least $2n$ CNOT gates, resulting in substantial resource overhead [38]. Recent developments have shown that simultaneous application of two CR gates combined with the Pancharatnam-Berry geometric phase [39], can produce more efficient gate constructions with durations as short as 353 ns [12]. As an alternative, directly harnessing the native PCR interaction based on $ZZX_{\pi/4}$, supplemented by two-qubit ZX operations, offers a compelling route toward reducing CNOT gate depth. Within this framework, the ideal Hamiltonian for realizing a CCNOT-like gate can be expressed as

$$\begin{aligned} H_{\mathrm{CCNOT}} &= -\frac{\pi}{8}(I_1 - Z_1)(I_2 - Z_2)(I_3 - X_3) \\ &= \frac{\pi}{8}\left[(IZI + ZII + IIX) + ZZX\right. \\ &\quad \left. -(ZZI + IZX + ZIX + III)\right] \\ &\simeq \begin{pmatrix} 1 & 0 & 0 & 0 & 0 & 0 & 0 & 0 \\ 0 & 1 & 0 & 0 & 0 & 0 & 0 & 0 \\ 0 & 0 & 1 & 0 & 0 & 0 & 0 & 0 \\ 0 & 0 & 0 & 1 & 0 & 0 & 0 & 0 \\ 0 & 0 & 0 & 0 & 1 & 0 & 0 & 0 \\ 0 & 0 & 0 & 0 & 0 & 1 & 0 & 0 \\ 0 & 0 & 0 & 0 & 0 & 0 & 0 & 1 \\ 0 & 0 & 0 & 0 & 0 & 0 & 1 & 0 \end{pmatrix}. \end{aligned} \tag{2}$$

In this construction, all contributing Pauli terms commute, enabling coherent evolution under their simultaneous action. Applying the associated unitary operator to a computational basis state $|q_1q_2q_3\rangle$ yields

$$U(H_{\mathrm{CCNOT}})\,|q_1q_2q_3\rangle = e^{im\frac{\pi}{8}}e^{-im\frac{\pi}{8}X_3}\,|q_1q_2q_3\rangle\,,$$

where the phase coefficient is given by $m = 1 + (-1)^{q_1+q_2} - (-1)^{q_1} - (-1)^{q_2}$. It is straightforward to verify that $m = 4$ if and only if $q_1 = q_2 = 1$, corresponding to control state $|11\rangle$; for all other control states ($|00\rangle$, $|01\rangle$, $|10\rangle$), one finds $m = 0$. Hence, m can be equivalently written as $4q_1q_2$, leading to the simplified unitary transformation:

$$U_{\mathrm{CCNOT}}\,|q_1q_2q_3\rangle = (1 - q_1q_2)\,|q_1q_2q_3\rangle + q_1q_2\,|q_1q_2\overline{q_3}\rangle\,.$$

This expression shows that for all control states except $|11\rangle$, the unitary reduces to identity. When $q_1 = q_2 = 1$, the third qubit flips, thereby implementing the standard CCNOT operation. To realize this gate via Hamiltonian engineering, one can construct an effective three-qubit

interaction satisfying:

$$\alpha_{ZZI} = \alpha_{IZX} = \alpha_{ZIX} = -\alpha_{ZZX}.$$

Under this condition, the CCNOT gate is implemented as a single-shot evolution under the resulting effective Hamiltonian, possibly supplemented by local single-qubit rotations.

In many practical scenarios, it is advantageous to consider a variant known as the *i*Toffoli gate, which omits stray *ZZ* interactions and admits a simpler form:

$$H_{i\text{Toffoli}} = \frac{\pi}{8}\left[(IIX + ZZX) - (IZX + ZIX)\right] \simeq \begin{pmatrix} 1 & 0 & 0 & 0 & 0 & 0 & 0 & 0 \\ 0 & 1 & 0 & 0 & 0 & 0 & 0 & 0 \\ 0 & 0 & 1 & 0 & 0 & 0 & 0 & 0 \\ 0 & 0 & 0 & 1 & 0 & 0 & 0 & 0 \\ 0 & 0 & 0 & 0 & 1 & 0 & 0 & 0 \\ 0 & 0 & 0 & 0 & 0 & 1 & 0 & 0 \\ 0 & 0 & 0 & 0 & 0 & 0 & 0 & i \\ 0 & 0 & 0 & 0 & 0 & 0 & i & 0 \end{pmatrix}. \quad (3)$$

Applying the associated unitary yields

$$U_{i\text{Toffoli}}\,|q_1q_2q_3\rangle = (1 - q_1q_2)\,|q_1q_2q_3\rangle - iq_1q_2\,|q_1q_2\overline{q_3}\rangle\,.$$

As before, this expression implies that the gate acts as identity unless both control qubits are in the $|1\rangle$ state. In the $|11\rangle$ configuration, the third qubit undergoes a bit flip with an additional $-i$ phase, consistent with the definition of an *i*Toffoli operation.

3. A CZZ gate for surface-code QEC

Quantum error correction (QEC) is essential for achieving fault-tolerant quantum computation. In surface-code architectures, stabilizer measurements are typically implemented through sequences of two-qubit gates, which can limit operation speed and introduce additional errors. Recent advances have proposed a three-qubit controlled-*Z*-*Z* (CZZ) gate that enables direct parity mapping of two data qubits onto a measurement qubit in a single step, thereby achieving higher error thresholds and lower logical error rates compared to the standard CZ-based readout [20,21]. In addition to its interpretation as two simultaneous CZ gates, the CZZ operation can also be realized via a direct three-body interaction, with the ideal Hamiltonian given by

$$H_{\text{CZZ}} = \begin{pmatrix} 1 & 0 & 0 & 0 & 0 & 0 & 0 & 0 \\ 0 & 1 & 0 & 0 & 0 & 0 & 0 & 0 \\ 0 & 0 & 1 & 0 & 0 & 0 & 0 & 0 \\ 0 & 0 & 0 & 1 & 0 & 0 & 0 & 0 \\ 0 & 0 & 0 & 0 & 1 & 0 & 0 & 0 \\ 0 & 0 & 0 & 0 & 0 & -1 & 0 & 0 \\ 0 & 0 & 0 & 0 & 0 & 0 & -1 & 0 \\ 0 & 0 & 0 & 0 & 0 & 0 & 0 & 1 \end{pmatrix} \simeq -\frac{\pi}{4}\,(I_1 - Z_1)\,Z_2Z_3 = -\frac{\pi}{4}\,(IZZ - ZZZ)\,. \quad (4)$$

The action of the corresponding unitary operator on a computational-basis state is

$$U_{\text{CZZ}}\,|q_1q_2q_3\rangle = e^{iq_1(-1)^{q_2+q_3}\frac{\pi}{2}}\,|q_1q_2q_3\rangle\,.$$

It is straightforward to verify that when the first qubit (measurement qubit) is in the control state $|1\rangle$, the odd-parity states of the last two qubits (data qubits), $|101\rangle$ and $|110\rangle$, acquire a nontrivial $+\pi/2$ phase shift, while the even-parity states, $|100\rangle$ and $|111\rangle$, acquire a $-\pi/2$ phase shift. This gate serves as a parity-check measurement primitive in the surface code, enabling the readout of *Z*-, *X*-, and *Y*-type stabilizers. Moreover, the Hamiltonian in Eq. (4) can be implemented via the PCR gate through the decomposition

$$U_{\text{CZZ}} = S_1^{\dagger}H_3U_{IZX}\left(\frac{\pi}{2}\right)U_{ZZX}\left(-\frac{\pi}{2}\right)H_3, \quad (5)$$

which requires the corresponding Pauli coefficients to satisfy $\alpha_{ZZX} = -\alpha_{IZX}$, while all other undesired terms are suppressed.

B. Implementation of *ZZX*

We have demonstrated that utilizing the PCR gate can effectively reduce circuit depth, as both the GHZ state and the *i*Toffoli gate can be implemented in a single shot. We now turn to the realization of the core three-qubit *ZZX* interaction underlying the PCR gate.

To implement this key mechanism, a minimal superconducting circuit requires only three qubits. In this work, we adopt the coupling strategy used in IBM Quantum's Eagle processors, which employ a heavy-hexagonal qubit layout. In this architecture, each qubit except those at the edges is coupled to two or three neighbors, forming a lattice reminiscent of tessellated hexagonal edges and vertices.

We focus on a representative three-qubit unit cell composed of qubits Q_1, Q_2, and Q_3, extracted from the architecture of the `ibm_sherbrooke` quantum processor, as illustrated in Fig. 1. Within this cell, each pair of neighboring qubits is connected through both a fixed capacitive

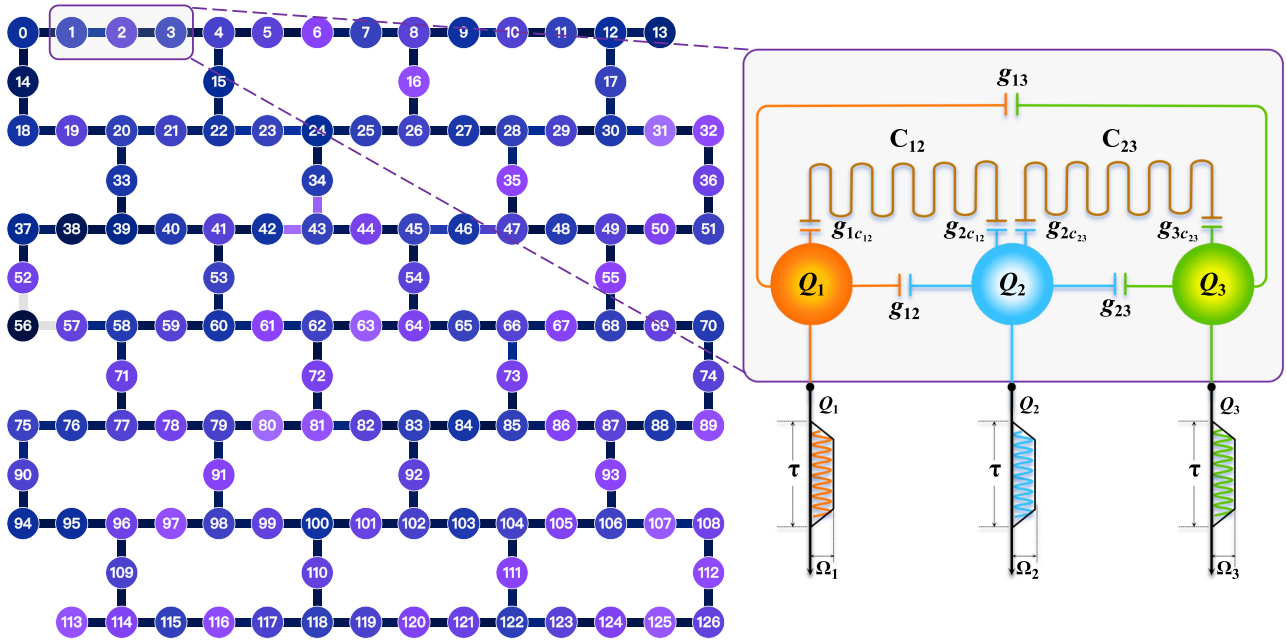

FIG. 1. Left: Physical layout of IBM's 127-qubit Eagle quantum processor, `ibm_sherbrooke`. Right: Circuit-level representation of a selected three-qubit segment (Q_1, Q_2, Q_3) from the Sherbrooke device.

coupling of strength g_{ij} $(i,j \in \{1,2,3\}, i \neq j)$ and a tunable intermediary coupler C_r $(r \in \{12,23\})$ with coupling strengths g_{iC_r} and g_{jC_r}. Notably, the terminal qubits Q_1 and Q_3 do not have dedicated tunable couplers and interact solely via their static capacitive link.

In the dispersive regime, where $g_{jC_r} \ll |\omega_{C_r} - \omega_{Q_j}|$ with ω_{C_r} denoting the coupler C_r frequency and ω_{Q_j} the qubit Q_j frequency, the circuit Hamiltonian can be reduced to the multilevel qubit basis as ($\hbar \equiv 1$)

$$\begin{aligned} H_{\rm cir} = & \sum_{Q_j=\{Q_1,Q_2,Q_3\}} \sum_{n_j} \bar{E}_{Q_j}(n_j)|n_j\rangle\langle n_j| \\ & + \sum_{Q_i,Q_j\,(i\neq j)} \sum_{m_i,n_j} \sqrt{(m_i+1)(n_j+1)} \\ & \times \mathcal{J}_{Q_iQ_j}\left(|m_i,n_j+1\rangle\langle m_i+1,n_j| + \text{H.c.}\right), \end{aligned} \tag{6}$$

where m_i and n_j are two energy levels in the qubits Q_i and Q_j. The quantity $\bar{\omega}_{Q_j}(n_j)$ is defined as the effective transition frequency between levels n_j and n_j+1, $\bar{\omega}_{Q_j}(n_j) = \bar{E}_{Q_j}(n_j+1) - \bar{E}_{Q_j}(n_j)$. The term $\mathcal{J}_{Q_iQ_j}$ denotes the set of effective coupling strength between qubit Q_i in state m_i and qubit Q_j in state n_j. When either $m_i \geq 1$ or $n_j \geq 1$, we explicitly indicate the excitation levels using index notation: interactions confined to the computational subspace are denoted as $J_{Q_iQ_j}$, those involving higher excited states as $J_{\overline{Q_iQ_j}}$, and mixed-state interactions as $J_{Q_i\overline{Q_j}}$. This notation extends naturally to higher excitation levels; for instance, interactions involving the third excited state are marked with a double overline, such as $J_{\overline{\overline{Q_iQ_j}}}$. For conciseness, we sometimes omit the "Q" label and refer solely to the qubit indices. Further details are available in Ref. [40].

The implementation of the three-qubit interaction follows a protocol analogous to the CR gate. For instance, qubits Q_1 and Q_3 serve as control qubits, while Q_2 is designated as the target. To induce the desired interaction, microwave drives are applied to all three qubits. Each qubit is driven at the dressed frequency of the target qubit Q_2, enabling effective control through higher-order interaction pathways. The general form of the drive Hamiltonian is expressed as

$$H_{\rm dr} = \sum_{j=1,2,3} \Omega_j \cos\left(\omega_{\rm dr}t + \phi_j\right)\left(\hat{b}_j + \hat{b}_j^\dagger\right), \tag{7}$$

with Ω_j is the driving amplitude applied on the qubit Q_j with the frequency $\omega_{\rm dr}$ and the phase ϕ_j. The operators $\hat{b}_j^\dagger$ ($\hat{b}_j$) is the creation (annihilation) operator for the qubit Q_j.

The total Hamiltonian is given by $H_{\rm tot} = H_{\rm cir} + H_{\rm dr}$. To extract the effective interaction relevant for quantum gate implementation, we move to a rotating frame defined by the dressed frequency of the target qubit Q_2 and apply the rotating-wave approximation (RWA) to eliminate fast-oscillating terms [41]. In this frame, the Hamiltonian becomes time-independent to leading order and is subsequently block diagonalized in the computational basis $\{|n_1,n_3,n_2\rangle\}$, where $n_j \in \{0,1\}$ indicates the occupation number of qubit Q_j.

TABLE I. Comparison of the proposed PCR gate with existing three-qubit cross-resonance-based gates.

	This work (PCR)	Ref. [12]	Ref. [22]
Model validation	Simulation	Experiment	Experiment
Target operation	GHZ/iToffoli/CCNOT/CZZ	iToffoli gate	SCRP gate
Topology	K_3 (complete graph)	P_3 (chain)	P_3 (chain)
Interaction type	ZZX (ZIX, IZX)	ZIX, IZX	ZIX, IZX
Operating regime	Strong/nondispersive	Dispersive	Dispersive
Optimization strategy	Search-based algorithm	Berry phase assisted	Echo pulse
Stray interaction suppression	Yes	No	Yes
Overhead	Static parameter search	Complex pulse sequences	Simultaneous calibration

Following block diagonalization, the effective Hamiltonian is then rewritten in the Pauli basis as

$$H_{\text{total}} = \sum_{\substack{A,B\in\{I,Z\}\\ C\in\{I,X,Y,Z\}}} \alpha_{ABC} A\otimes B\otimes C. \tag{8}$$

Here, each coefficient α_{ABC} quantifies the contribution of the corresponding Pauli operator ABC in the effective Hamiltonian. Among these terms, particular attention is devoted to the ZZX component, which represents a genuine three-qubit interaction and constitutes the central focus of our engineering efforts. The objective is to modulate the strength of α_{ZZX} while minimizing the amplitudes of all other undesired components. A perturbative analysis based on the Schrieffer-Wolff transformation (SWT) [42], truncated at first order in the drive amplitude Ω, allows for analytical derivation of these effective interaction terms. The details of this derivation are provided in Appendix A.

In the dispersive regime, the intrinsic strength of the three-body ZZX interaction typically scales as $J^2\Omega/\Delta^2$, rendering it significantly weaker than two-body cross terms like ZIX and IZX, which scale more favorably as $J\Omega/\Delta$. This hierarchy reflects the general suppression of higher-order terms predicted by many-body localization theory [43–45], where multiqubit interactions arise perturbatively and thus appear with reduced amplitude. As a result, engineering strong ZZX interactions requires deliberate circuit design strategies that go beyond the standard dispersive approximation. These include the following: (i) ensuring all three qubits are appreciably coupled, (ii) tuning pairwise detunings into the straddling regime, and (iii) precisely biasing the couplers to access the desired interaction manifold. Recent proposals offer a promising alternative to single-mode tunable couplers: by employing multimode coupler architectures, one can significantly enhance effective multiqubit interactions within more sophisticated circuit layouts [46]. Table I compares the proposed PCR gate with previously demonstrated three-qubit gates based on simultaneous cross-resonance drives. The key distinction is that the proposed method exploits a strong direct three-body ZZX interaction beyond the dispersive regime, whereas the other gates operate in the dispersive regime and rely solely on simultaneous two-body interactions.

III. GRADIENT-FREE OPTIMIZATION FRAMEWORK

To enable high-fidelity three-qubit PCR gate, this section introduces a practical optimization framework designed to selectively amplify the ZZX interaction while suppressing undesired terms. The methodology integrates phase calibration, perturbative initialization, and a gradient-free nonperturbative optimization routine to shape the interaction profile within experimentally accessible constraints.

The procedure begins with calibrating the drive phases ϕ_1, ϕ_2, and ϕ_3 to either 0 or π. This phase configuration ensures that all Y-type terms in the effective Hamiltonian are eliminated, thereby simplifying the underlying interaction structure and facilitating both analytical tractability and numerical stability.

Following phase calibration, a perturbative analysis is employed to generate an initial estimate for the circuit parameters that favor the emergence of the ZZX term. This initial configuration, derived from analytical expressions valid in the weak-coupling regime, serves as a guided starting point for the subsequent nonperturbative optimization process. Together, these steps establish a robust foundation for efficiently engineering the desired three-body interaction.

Nevertheless, perturbation theory becomes inadequate in regimes where higher-order effects are significant—particularly near the optimal working point, where nonlinear interactions can no longer be ignored. To overcome these limitations and achieve high-fidelity performance, we adopt a *nonperturbative numerical block-diagonalization method*, based on the *principle of least action* [28,47], which has been modified and implemented in our software package **CirQubit** [48]. In our simulations, qubits and couplers are modeled with a maximum total excitation number of four, since results are unchanged for higher excitation numbers, see details in Appendix A. This setting is sufficient for the current

three-qubit plus two-coupler configurations, and results remain stable under variations in the excitation cutoff.

When selecting the optimization strategy for variational parameter tuning, we systematically compare four representative methods: the gradient-free Powell algorithm, Bayesian optimization, the Nelder-Mead simplex method, and the gradient-based L-BFGS-B algorithm. This comparison aims to assess both the convergence efficiency and the accuracy of the resulting quantum states. To provide a quantitative evaluation, we compute the GHZ-state fidelity obtained using the optimized parameters across all unit cells (see details in Sec. IV A). The numerical results and fidelity distributions corresponding to different fidelity thresholds are summarized in Fig. 2. All optimization procedures are performed under identical computational conditions on an Apple MacBook Pro (2024) equipped with an Apple M4 Pro chip (14-core CPU, 20-core GPU), 24-GB unified memory, and running macOS 15.5.

Figure 2 presents a comparative analysis of the four optimization methods in terms of GHZ-state fidelity distributions across all unit cells. For quantitative reference, the proportions of unit cells achieving fidelities above 50%, 90%, and 99% are as follows: Powell (69.6%, 31.9%, 8.7%), Bayesian optimization with 200 evaluations (34.8%, 11.6%, 0.0%), Nelder-Mead (75.4%, 31.9%, 10.1%), and L-BFGS-B (66.7%, 27.5%, 8.7%). Among these, Bayesian optimization exhibits the weakest overall performance, while the gradient-free Powell algorithm achieves a comparable fidelity distribution to Nelder-Mead and L-BFGS-B.

Of note, the Powell method attains this level of performance with the shortest runtime, averaging approximately 3.5 min per optimization, in contrast to the substantially longer runtimes of the Nelder-Mead (35 min) and L-BFGS-B (84 min) methods.

Given its favorable trade-off between computational efficiency and accuracy, we adopt the gradient-free conjugate-direction Powell method as our primary optimizer. Its low computational overhead and robustness to stochastic noise make it particularly effective for mitigating the barren plateau problem, especially in near-resonant regimes where gradient-based optimizers often suffer from vanishing signal gradients.

Therefore, the optimization loop employing the Powell algorithm proceeds through the following sequence of steps:

(a) **Initialization from perturbative estimates**: The process begins with perturbative analysis of a targeted Hamiltonian by estimating circuit parameters such as coupler frequencies and driving amplitude. These estimates provide an informed starting point that guides the optimization toward parameter regimes conducive to strong target interactions.

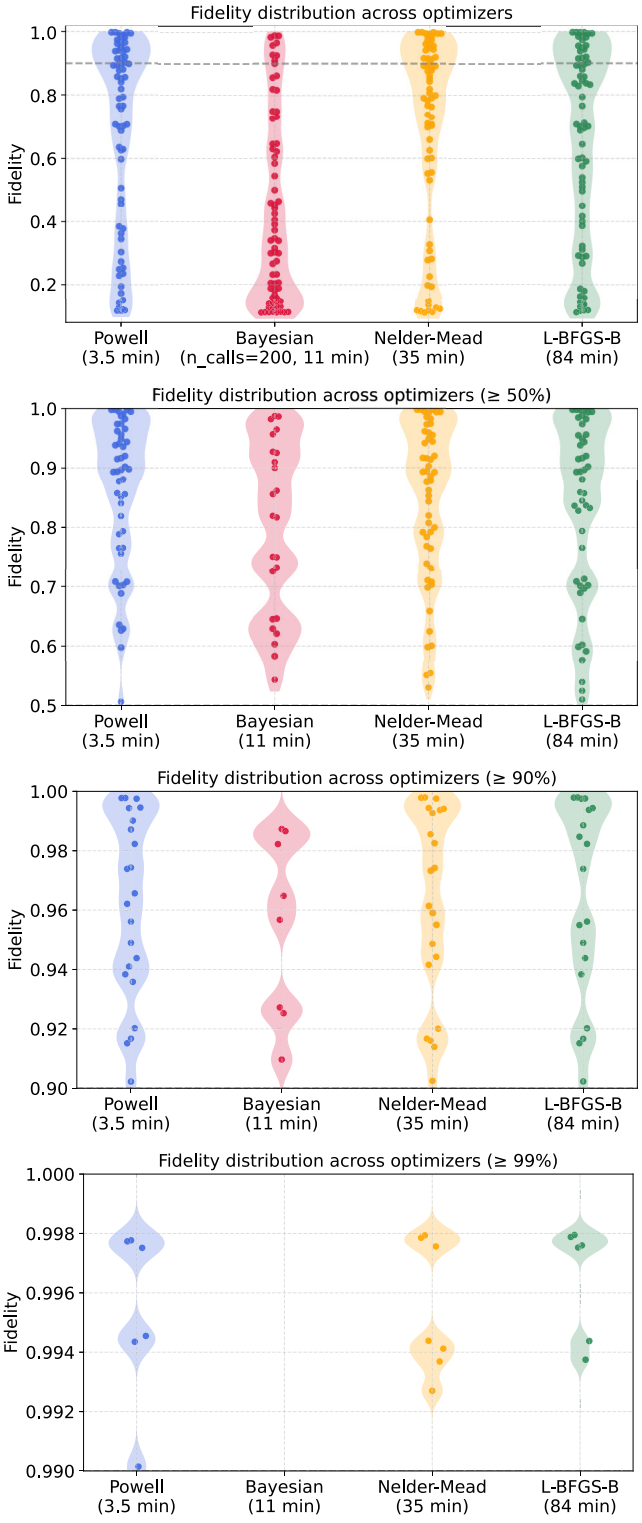

FIG. 2. Comparison of GHZ-state fidelities obtained using different optimization methods: gradient-free Powell, Bayesian optimization, Nelder-Mead, and gradient-based L-BFGS-B. The panels display the fidelity distributions for (1) the full range of F, (2) $F > 0.5$, (3) $F > 0.9$, and (4) $F > 0.99$. All optimization runtimes were benchmarked on an Apple MacBook Pro (2024) equipped with an Apple M4 Pro chip (14-core CPU, 20-core GPU), 24 GB unified memory, and macOS 15.5.

(b) **Gradient-free exploration**: A gradient-free heuristic optimization algorithm Powell is used to efficiently navigate the search in the high-dimensional parameter space. The goal is to increase the strength of the desired Pauli term, such as the *ZZX* interaction, while simultaneously suppressing all unwanted components in the effective Hamiltonian.

(c) **Nonperturbative Hamiltonian evaluation**: At each step of the optimization, the effective Hamiltonian is reconstructed using the nonperturbative technique. This method accounts for higher-order effects and nonlinearities that are not captured by perturbation theory, ensuring accurate characterization of the system's dynamics [48].

(d) **Cost-function-driven refinement**: The optimization search model iteratively updates the circuit parameters by minimizing a tailored cost function. This function penalizes contributions from undesired Pauli terms and rewards configurations that reinforce the target interaction, thereby guiding the system toward an optimized Hamiltonian structure.

This optimization is guided by a carefully designed cost function that balances the enhancement of the wanted terms with the suppression of unwanted interactions:

$$\mathcal{L}_{\text{total}} = \mathcal{L}_{\text{wanted}} + \mathcal{L}_{\text{unwanted}} + \mathcal{L}_{\text{constraint}}, \tag{9}$$

where $\mathcal{L}_{\text{wanted}}$ promotes strong, nontrivial desired interactions, $\mathcal{L}_{\text{unwanted}}$ penalizes the presence of undesired Pauli components, and $\mathcal{L}_{\text{constraint}}$ ensures that the circuit parameters remain within a physically valid regime.

Algorithm 1 outlines the workflow and structure of the Powell search method, with the output corresponding to an optimized set of circuit parameters.

It is worth noting that our search-based approach differs conceptually from quantum optimal control methods, such as GRAPE [49], CRAB [50], and GOAT [51]. Quantum optimal control treats control amplitudes as continuous functions of time and typically employs gradient-based algorithms to maximize gate or state fidelity under physical constraints. In contrast, the present framework focuses on identifying optimal static operating parameters, specifically the tunable coupler frequency and driving amplitude, by exploring the space of experimentally accessible conditions. We regard quantum optimal control as a complementary and natural extension of our approach, which can be applied after suitable operating points are identified to further refine the control protocol and enhance fidelity.

ALGORITHM 1. Powell optimization algorithm.

Input: Target Pauli term (e.g., ZZX), initial circuit parameters $\mathbf{x}_0 \in \mathbb{R}^n$, loss threshold ε, maximum iterations
Initialization: Estimate $\mathbf{x}_0$ from perturbative analysis
Set direction set: $\{\mathbf{d}_1, \ldots, \mathbf{d}_n\} \leftarrow \{\mathbf{e}_1, \ldots, \mathbf{e}_n\}$ (standard basis)
while not converged **and** iteration count $<$ max iterations **do**
  $\mathbf{x} \leftarrow \mathbf{x}_0$
  for $i \leftarrow 1$ **to** n **do**
    Define cost function: $\phi_i(\alpha) \leftarrow \mathcal{L}_{\text{total}}(\mathbf{x} + \alpha \mathbf{d}_i)$
    Find optimal step: $\alpha_i^* \leftarrow \arg\min_\alpha \phi_i(\alpha)$
    Update parameters: $\mathbf{x} \leftarrow \mathbf{x} + \alpha_i^* \mathbf{d}_i$
    Evaluate effective Hamiltonian: $\hat{H}_{\text{eff}} \leftarrow$ CirQubit.NonperturbativeSolver($\mathbf{x}$)
  end for
  Compute displacement: $\mathbf{u} \leftarrow \mathbf{x} - \mathbf{x}_0$
  Define: $\phi_u(\alpha) \leftarrow \mathcal{L}_{\text{total}}(\mathbf{x}_0 + \alpha \mathbf{u})$
  Find: $\alpha^* \leftarrow \arg\min_\alpha \phi_u(\alpha)$
  Update point: $\mathbf{x}_{\text{new}} \leftarrow \mathbf{x}_0 + \alpha^* \mathbf{u}$
  Identify longest step: $j \leftarrow \arg\max_i \|\alpha_i^* \mathbf{d}_i\|$
  Replace direction: $\mathbf{d}_j \leftarrow \mathbf{u}$
  if $\|\mathbf{x}_{\text{new}} - \mathbf{x}_0\| < \varepsilon$ **then**
    break
  else
    $\mathbf{x}_0 \leftarrow \mathbf{x}_{\text{new}}$
  end if
end while
Output: Optimized parameters $\mathbf{x}_{\text{new}}$ realizing strong target interaction

IV. VALIDATION OF THE OPTIMIZATION ALGORITHM

To ensure the reliability and effectiveness of the proposed optimization framework, we conduct a detailed validation using two representative applications: the generation of a three-qubit GHZ state and the implementation of an *i*Toffoli gate. These benchmarks illustrate the practical advantages of the optimized PCR gate in realistic settings. For each case, we simulate the time evolution of the system governed by the effective Hamiltonian derived from the optimized circuit parameters. The simulations incorporate each single-qubit gate duration of 30 ns and include decoherence effects modeled using the experimentally measured coherence times of the target quantum processor. The results therefore do not include SPAM errors or other experimental imperfections such as calibration errors or TLS defects.

To further validate the method under device-specific conditions, we apply the optimization algorithm to the `ibm_sherbrooke` quantum processor, leveraging its scalable architecture to organize qubits into optimized three-qubit unit cells. In particular, we assume a virtual nonzero direct coupling g_{13} to enhance the three-qubit interaction; details are provided in Appendix A. Each unit cell is indexed by n and labeled according to its central qubit, as illustrated in Fig. 1.

While IBM's Eagle-generation processors utilize fixed-frequency harmonic resonators to mediate qubit interactions, the newer Heron architecture introduces tunable couplers, offering greater flexibility in engineering interaction strengths. Accordingly, in our simulations, we adopt

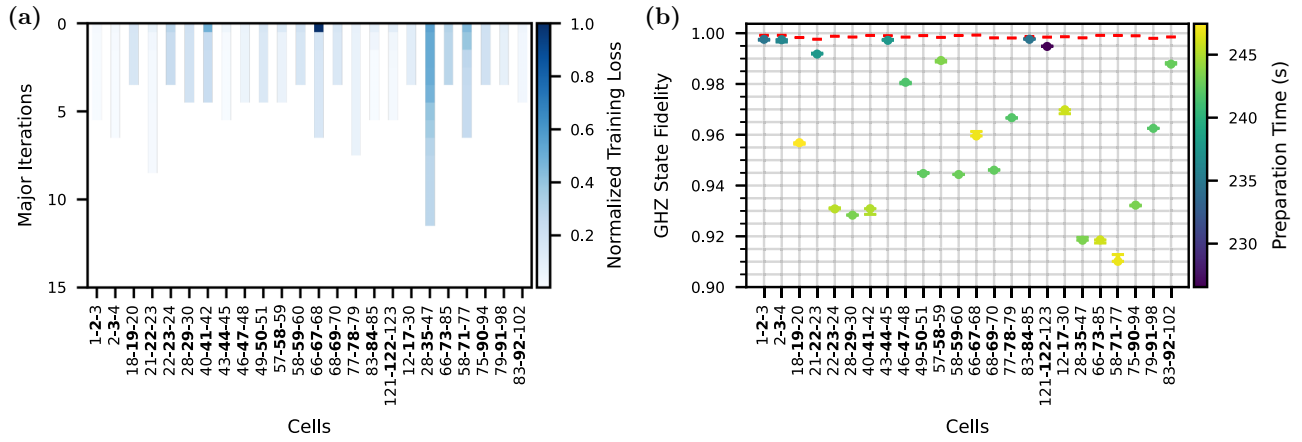

FIG. 3. Benchmarking GHZ state preparation on the `ibm_sherbrooke` processor. (a) Normalized optimization loss versus major iterations, where each iteration updates all parameter search directions once. (b) GHZ fidelity for selected three-qubit unit cells using optimized PCR gates ($ZZX_{\pi/2}$) under realistic noise. The colorbar shows evolution time; the red slash marks the coherence limit. Error bars reflect ±2% drive parameter and ±5 MHz coupler frequency perturbations. Q_2 is selected as the **target** qubit to satisfy the ZX-like constraint.

the following assumptions: qubit frequencies and anharmonicities are held constant, and static coupling strengths are inferred from calibrated ZZ interaction values reported in the processor properties. Under these constraints, the optimization is performed over a reduced set of control variables, namely the drive amplitudes Ω_1, Ω_2, and Ω_3, along with the coupler frequencies $\omega_{C_{12}}$ and $\omega_{C_{23}}$.

To further simplify the optimization landscape, we fix $\Omega/2\pi = 60$ MHz and treat the drive amplitudes of all three qubits in terms of relative scaling factors, defined as $A_1 = \Omega_1/\Omega$, $A_2 = \Omega_2/\Omega$ and $A_3 = \Omega_3/\Omega$. This reparameterization reduces the dimensionality of the search space, facilitating a more efficient and tractable optimization process. The corresponding initialization procedure is detailed in Appendix B.

A. Example 1: GHZ state fidelity

To generate a three-qubit GHZ state, the desired interaction is exclusively of the ZZX type, while all other terms are considered unwanted. We evaluate a total of 69 distinct three-qubit circuit configurations, applying the optimization procedure independently to each, using the basis ordering $|Q_1, Q_3, Q_2\rangle$. Here, we define the target interaction as $\mathcal{L}_{\text{wanted}} = \mathcal{L}_{ZZX}$, and the resulting training loss across all configurations is summarized in Fig. 3(a).

To assess the fidelity of the generated GHZ state, we first validate the optimization results by substituting the optimized parameters back into the nonperturbative framework to recalculate the effective Pauli coefficients using our software CirQubit [48], corresponding result is presented in Fig. 8. These coefficients are subsequently used to reconstruct the full effective Hamiltonian as defined in Eq. (8). We then simulate the time evolution of the initial state $|000\rangle$ under the reconstructed Hamiltonian using corresponding pulse sequences. The PCR gate is implemented using a flat-top Gaussian pulse of duration τ, with 10-ns rise and fall times. Thus, the total implementation time is $t_{\text{GHZ}} = (2 \times 30 + \tau)$ ns, where the two 30-ns single-qubit gates are applied before and after the PCR gate. The fidelity of the resulting state is evaluated by solving the Lindblad master equation. Note that although the optimization is performed under a fixed driving amplitude Ω, the targeted cost function may still hold as long as the Pauli coefficients scale linearly with the drive amplitude [52]. Therefore, the simulation is repeated over a range of Ω values, and the maximum fidelity is extracted from the evaluated steps. This protocol provides a quantitative assessment of the effectiveness of the ZZX-based entangling operation and identifies the optimal parameters for high-fidelity GHZ state preparation.

Figure 3(b) shows that more than one third of the 69 evaluated unit cells achieve GHZ state fidelities above 90%, with 6 unit cells exceeding 99% fidelity, demonstrating that the optimized PCR gate consistently enables high-fidelity entanglement. Notably, these high-fidelity states are realized within a total evolution time of 250 ns, underscoring the protocol's robustness and efficiency across diverse hardware configurations. The dominant source of infidelity arises from parasitic stray interactions; however, for unit cells attaining fidelities above 99%, dynamic ZZ cancellation effectively eliminates such parasitic effects [53], resulting in a nearly parasitic-free gate [52].

To assess the protocol's robustness against experimental imperfections, we introduce random perturbations of ±2% to the optimized drive parameters and ±5 MHz to the coupler frequencies, with fidelity variations depicted as asymmetric errorbars. The results indicate that only configurations with slightly lower baseline fidelities

exhibit sensitivity to these perturbations, while the majority remain largely unaffected. These findings validate the feasibility of implementing native three-qubit gate synthesis on current superconducting quantum hardware.

After generating the GHZ state using the optimized ZZX interaction and corresponding pulse sequence, we evaluate the stability and quality of the resulting entangled state under realistic post-preparation conditions. Once the driving amplitudes are turned off, the system is left to evolve under residual static interactions and decoherence. These parasitic effects, if not properly accounted for, can lead to fidelity degradation [53–58].

To assess the impact of residual coherent interactions, we consider the static part of the effective Hamiltonian derived from the optimized parameters $H_{\text{static}} = \alpha_{ZZI} ZZI + \alpha_{ZIZ} ZIZ + \alpha_{IZZ} IZZ + \alpha_{ZZZ} ZZZ$. The time evolution of an ideal GHZ state under this static Hamiltonian H_{static} leads to the following state after a duration τ_p:

$$\text{GHZ}(\tau_p)\rangle = \frac{e^{-i\alpha_{ZZZ}\tau_p}|000\rangle + e^{i\alpha_{ZZZ}\tau_p}|111\rangle}{\sqrt{2}}. \tag{10}$$

Interestingly, two-body terms such as ZZI, ZIZ, and IZZ contribute equally to both $|000\rangle$ and $|111\rangle$, resulting in a global phase that does not alter the quantum state. This is due to the even parity of these operators with respect to the GHZ basis states. In contrast, the ZZZ term introduces a relative phase between the $|000\rangle$ and $|111\rangle$ components due to its odd parity, leading to coherent phase accumulation. Therefore, characterizing and, if necessary, correcting for the ZZZ-induced phase shift is essential for maintaining high-fidelity operation in downstream quantum information processing tasks.

One practical approach to mitigate the coherent phase accumulation caused by the ZZZ term is to apply a compensating time-dependent phase correction. This can be achieved, for instance, by implementing a single-qubit Z rotation on any one of the three qubits. Specifically, applying a Z rotation of angle $\alpha_{ZZZ}t$ effectively cancels the relative phase between the $|000\rangle$ and $|111\rangle$ components, restoring the ideal GHZ state. This correction is especially useful when the accumulated phase is deterministic and the interaction strength α_{ZZZ} is well characterized.

B. Example 2: CCNOT-like gate fidelity

1. *i*Toffoli *gate*

To enable fast and efficient implementation of the *i*Toffoli gate, we employ a single-shot pulse protocol wherein circuit parameters are optimized to satisfy the symmetry condition $\alpha_{ZZX} = \alpha_{IIX} = -\alpha_{ZIX} = -\alpha_{IZX}$, while simultaneously suppressing all undesired Pauli terms in the effective Hamiltonian. This engineered interaction realizes a native three-qubit gate in the computational basis ordered as $|Q_1, Q_3, Q_2\rangle$, where qubit Q_2 acts as the target and Q_1, Q_3 serve as the controls.

The optimization procedure mirrors that used for GHZ state generation, except that the cost function is replaced with $\mathcal{L}_{i\text{Toffoli}}$, designed specifically to enforce the desired ZX-like interaction structure. The optimization loss trajectory is presented in Fig. 4(a), and verification of the extracted Pauli coefficients for effective Hamiltonian reconstruction is shown in Fig. 9. The gate is implemented using a flat-top Gaussian pulse envelope, with total duration $t_{i\text{Toffoli}}$ ns.

2. CCNOT *gate*

The presence of a direct capacitive coupling g_{13} introduces a parasitic ZZ interaction. While this term can impair *i*Toffoli fidelity, it enables an alternative route to implementing a CCNOT gate. In addition to the symmetry conditions required for the *i*Toffoli gate, the CCNOT construction imposes $\alpha_{ZZI} = \alpha_{ZIX}$ and requires calibrated single-qubit rotations on both control qubits, as specified in Eq. (2). The total gate duration is extended to $t_{\text{CCNOT}} = (\tau + 30)$ ns.

To take advantage of this interaction structure, we retrain unit cells that did not achieve high-fidelity *i*Toffoli gates, now targeting CCNOT gate optimization. The corresponding training losses and reconstructed Hamiltonian coefficients are shown in Figs. 5(a) and 10, respectively.

Our benchmark spans 69 three-qubit unit cells on the `ibm_sherbrooke` architecture. For the *i*Toffoli gate, 16 configurations reach fidelities exceeding 90%, with over half completing within 200 ns—well within superconducting qubit coherence times, as shown in Fig. 4(b). In cases where parasitic ZZ interactions degrade *i*Toffoli performance, we repurpose those cells for CCNOT gates. Under an additional symmetry constraint and with postprocessed single-qubit rotations, 15 configurations achieve fidelities above 90%, as illustrated in Fig. 5(b). Notably, 3 unit cells for the *i*Toffoli and 4 for the CCNOT exceed 99% fidelity.

In both cases, the gates exhibit robustness to experimental imperfections: random perturbations of $\pm 2\%$ in drive amplitudes and ± 5 MHz in coupler frequencies lead to only marginal fidelity reductions. These results underscore the versatility and resilience of ZX-like interaction engineering for realizing high-fidelity, low-latency native multiqubit gates in superconducting quantum processors.

C. Example 3: CZZ gate

To realize a fast and efficient CZZ gate, we adopt a single-shot pulse protocol in which circuit parameters are optimized to satisfy the symmetry condition $\alpha_{ZZX} = -\alpha_{IZX}$, while simultaneously suppressing all other undesired Pauli terms in the effective Hamiltonian. The resulting interaction implements a native three-qubit gate in the computational basis ordered as $|Q_1, Q_3, Q_2\rangle$, where Q_1 serve as measure qubit, Q_2 and Q_3 act as the data qubit.

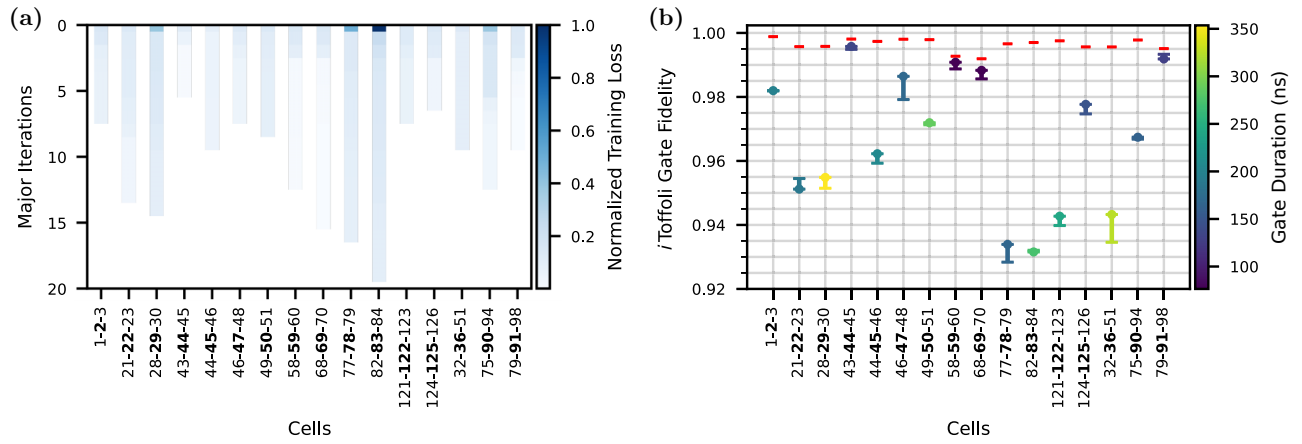

FIG. 4. Benchmarking three-qubit *i*Toffoli gate on the `ibm_sherbrooke` processor. (a) Normalized optimization loss versus major iterations, where each iteration updates all parameter search directions once. (b) *i*Toffoli gate fidelity for selected three-qubit unit cells using optimized ZX-like interaction under realistic noise. The colorbar shows evolution time; the red slash marks the coherence limit. Error bars reflect ±2% drive parameter and ±5 MHz coupler frequency perturbations. Qubit Q_2 is the **target**.

The optimization procedure follows that of the CCNOT-like gate, but with the cost function replaced by $\mathcal{L}_{\mathrm{CZZ}}$, which is tailored to enforce the desired ZZX and IZX interaction structure. The optimization loss trajectory is shown in Fig. 6(a), while Fig. 11 presents the extracted Pauli coefficients from effective Hamiltonian reconstruction. The gate is driven by a flat-top Gaussian pulse envelope with a total duration $t_{\mathrm{CZZ}} = (\tau + 2 \times 30)$ ns, where Hadamard and S gates are applied before and after the PCR gate, each with a duration of 30 ns.

Benchmarking results indicate that 11 out of 69 unit cells are capable of implementing the CZZ gate with a fidelity exceeding 90%. The average gate duration is approximately 350 ns, which is slightly longer than that of the CCNOT gate. The dominant error contributions arise from parasitic interactions, notably ZZI and ZIZ. Furthermore, random parameter drifts do not significantly affect the performance, demonstrating that the protocol is robust against such variations.

Although this work is primarily based on simulation, the proposed PCR gate is designed using realistic device parameters relevant to current superconducting qubit architectures, without requiring alternative circuit designs or extreme power levels. Challenges such as microwave calibration, power limitations, and frequency crowding are common to multiqubit processors [59,60], but they do not preclude the possibility of implementing the PCR gate experimentally.

The proposed method benefits from increased connectivity, as stronger direct multiqubit interactions can be realized in modular or highly connected architectures where qubit modules are coupled via common resonators

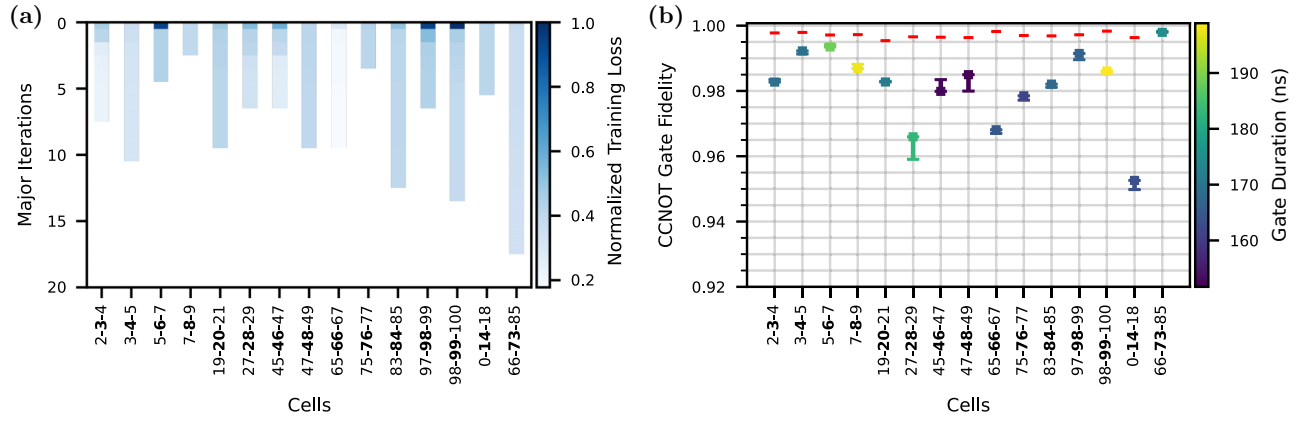

FIG. 5. Benchmarking three-qubit CCNOT gate on the `ibm_sherbrooke` processor. (a) Normalized optimization loss versus major iterations, where each iteration updates all parameter search directions once. (b) CCNOT gate fidelity for selected three-qubit unit cells using optimized ZX-like interaction under realistic noise. The colorbar shows evolution time; the red slash marks the coherence limit. Error bars reflect ±2% drive parameter and ±5 MHz coupler frequency perturbations. Qubit Q_2 is the **target**.

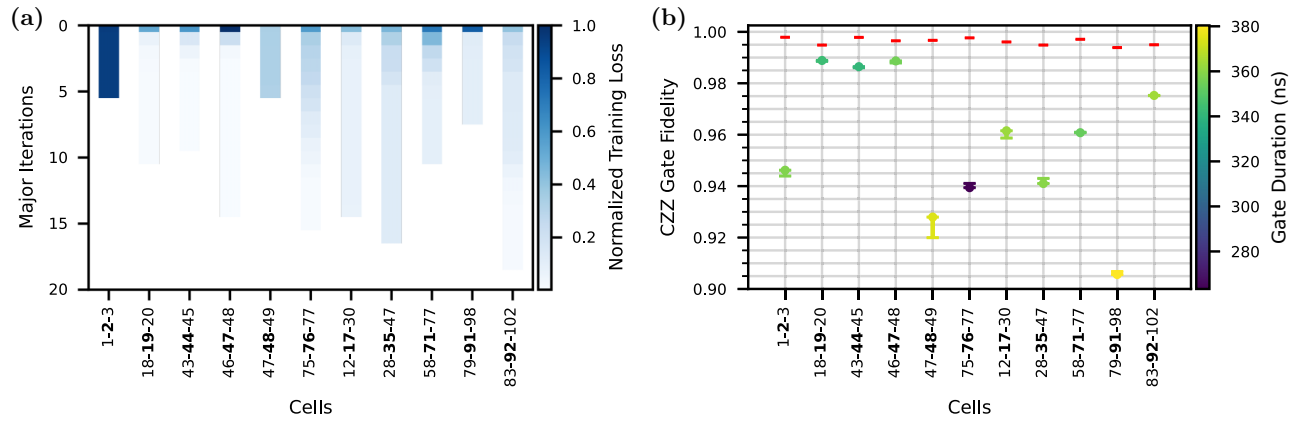

FIG. 6. Benchmarking three-qubit CZZ gate on the `ibm_sherbrooke` processor. (a) Normalized optimization loss versus major iterations, where each iteration updates all parameter search directions once. (b) CZZ gate fidelity for selected three-qubit unit cells using optimized *ZZX* and *IZX* interaction under realistic noise. The colorbar shows evolution time; the red slash marks the coherence limit. Error bars reflect ±2% drive parameter and ±5 MHz coupler frequency perturbations. Q_1 serves as the measure qubit while Q_2 and Q_3 act as the data qubits.

or waveguides. The search-based optimization provides a flexible framework for identifying optimal static operating points and suppressing stray interactions, suggesting that the PCR gate can be extended to larger systems and alternative coupling topologies while maintaining high fidelity.

The dominant sources of error in this work arise from parasitic couplings and decoherence effects. Further performance improvements can be achieved by combining the approach with quantum optimal control techniques, which can effectively suppress leakage to higher-energy levels.

V. CONCLUSION

We have introduced and validated a native three-qubit entangling gate—the parity cross-resonance (PCR) gate—that selectively amplifies the intrinsic *ZZX* interaction in fixed-frequency superconducting qubit platforms. In contrast to conventional approaches that decompose multiqubit operations into sequences of two-qubit gates, the PCR gate performs control–control–target and related unitaries in a single coherent step, reducing circuit depth and error accumulation.

A hybrid optimization framework, combining analytical perturbative modeling with nonperturbative, gradient-free tuning, enables selective enhancement of the desired *ZZX* term while suppressing spurious couplings. This approach yields robust performance across computational and higher-excitation subspaces, making the gate suitable for diverse applications: GHZ triplet state preparation, Toffoli-class logic, and a native controlled-*ZZ* (CZZ) operation that directly maps the parity of two data qubits onto a measurement qubit for faster, higher-fidelity stabilizer measurements in surface-code quantum error correction.

Simulations on selected 69 unit-cell configurations from IBM's heavy-hex architecture show that multiple subsets of unit cells achieve fidelities above 90%, several exceed 99%, and operate within sub-400 ns durations—well within coherence limits. Moreover, the achieved fidelities are not fundamental limits of the architecture. Further improvements are expected for circuits composed exclusively of fully tunable devices when combined with advanced optimal control techniques, which can more effectively suppress crosstalk and mitigate control imperfections.

These results demonstrate that higher-order interactions, often regarded as parasitic, can be repurposed into reliable, scalable primitives. This work lays the foundation for co-designing circuit architectures and control protocols that natively exploit multiqubit interactions, advancing the scalability and efficiency of next-generation superconducting quantum processors.

ACKNOWLEDGMENTS

This research received funding from the Horizon Europe OpenSuperQPlus100 project (Grant Agreement No. 101113946).

DATA AVAILABILITY

The data that support the findings of this article are not publicly available because they contain commercially sensitive information. The data are available from the authors upon reasonable request.

APPENDIX A: CIRCUIT HAMILTONIAN

In the circuit design, qubits are represented by circles and labeled as Q_j, where $j \in \{1, 2, 3\}$. The lumped *LC*

series symbolize the couplers, denoted by C_r, with $r = \{12, 23\}$, indicating the two qubits they mutually couple. The coupling strength between a qubit Q_j and a coupler C_r is represented as g_{jC_r}. Qubits interact indirectly through their shared coupler, while they can also experience direct interactions, such as capacitive coupling. The direct coupling strength between qubit Q_i and another qubit Q_j is denoted by g_{ij}.

For simplicity in our analysis, we assume that all couplers behave as harmonic oscillators, similar to transmission lines or cavity modes. In the model for Fig. 1, we neglect weak interactions between qubits and distant couplers as well as coupler-coupler interaction. Specifically, we set $g_{1C_{23}}/2\pi = g_{2C_{13}}/2\pi = g_{3C_{12}}/2\pi = 90$ MHz and $g_{12}/2\pi = g_{23}/2\pi = g_{13}/2\pi = 9$ MHz. While the direct coupling between the outer qubits is negligible in the `IBM_sherbrooke` layout, we assume that g_{13} is engineered to be as strong as the capacitive couplings between adjacent qubits, in order to enhance the three-body ZZX interaction. Under this assumption, the circuit Hamiltonian can be expressed as follows:

$$H_{\rm sys} = \sum_j \omega_j \hat{b}_j^\dagger \hat{b}_j + \frac{\delta_j}{2}\hat{b}_j^\dagger \hat{b}_j(\hat{b}_j^\dagger \hat{b}_j - 1) + \sum_r \omega_{C_r}\hat{a}_r^\dagger \hat{a}_r + \sum_{j,r} g_{jC_r}(\hat{b}_j - \hat{b}_j^\dagger)(\hat{a}_r - \hat{a}_r^\dagger) + \sum_{i\neq j} g_{ij}(\hat{b}_i - \hat{b}_i^\dagger)(\hat{b}_j - \hat{b}_j^\dagger) \tag{A1}$$

with ω_j being qubit bare frequency, δ_j qubit anharmonicity, and ω_{C_r} coupler frequency. In order to obtain the analytical Hamiltonian between qubits in the computational subset, first we restrict circuit parameters within the dispersive regime, i.e., $g_{jC_r} \ll |\omega_{C_r} - \omega_j|$, and using rotating-wave approximation (RWA), which helps to make the Hilbert space of harmonic couplers separable from qubit subset, therefore couplers can be safely eliminated and their effect renormalizes bare qubit frequency into their dressed values $\bar{\omega}_j(n_j) = \bar{E}_j(n_j + 1) - \bar{E}_j(n_j)$, with dressed state energies $\bar{E}_j(n_j)$ defined as

$$\bar{E}_j(n_j) = n_j\omega_j + \frac{n_j(n_j-1)}{2}\delta_j - \sum_r \frac{g_{jC_r}^2 n_j}{\Delta_{C_rj}(n_j - 1)},$$

with r summing over those resonators that interact with qubit Q_j via g_{jC_r}, and $\Delta_{C_rj}(n_j) \equiv \omega_{C_r} - \omega_j - n_j\delta_j$.

Two qubits Q_i and Q_j that share the same coupler C_r and couple to it by the strengths g_{iC_r} and g_{jC_r}, effectively interact with one another by the following effective strength:

$$\mathcal{J}_{ij} = g_{ij} - \frac{g_{iC_r}g_{jC_r}}{2}\left(\frac{1}{\Delta_{C_ri}(m_i)} + \frac{1}{\Delta_{C_rj}(n_j)}\right), \tag{A2}$$

with g_{ij} being direct coupling strength between the two qubits and the second term being the perturbative indirect coupling strength via the shared coupler.

By block diagonalizing the total Hamiltonian, the off-diagonal Pauli coefficients are evaluated perturbatively to first order in the drive amplitudes Ω_j. To further streamline the expressions, we introduce an overline notation to distinguish detunings and interactions involving noncomputational states: interactions confined to the computational

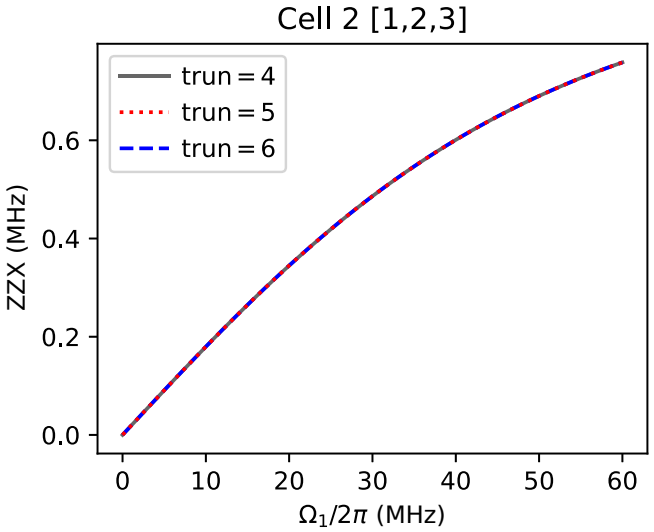

FIG. 7. ZZX values for different maximum excitation numbers in unit cell 2 during GHZ state implementation.

TABLE II. Initial parameters used in the optimization algorithm for GHZ state generation, *i*Toffoli and CZZ gate implementation in unit cell 2 ([1, 2, 3]), as well as for CCNOT gate realization in unit cell 3 ([2, 3, 4]).

	GHZ state	*i*Toffoli gate	CCNOT gate	CZZ gate
$\omega_{c_{12}}/2\pi$ [GHz]	5.321	5.301	5.301	5.301
$\omega_{c_{23}}/2\pi$ [GHz]	5.725	5.611	5.003	5.649
A_1	0.060	−0.311	0.174	−0.061
A_2	−0.007	0.015	0.010	0.005
A_3	1.500	−1.213	−0.016	−1.500

TABLE III. Physical constraints of parameters.

	Constraint
$\omega_{c_{12}}/2\pi$ [GHz]	[4.9, 7.0]
$\omega_{c_{23}}/2\pi$ [GHz]	[4.9, 7.0]
A_1	[−1.5, 1.5]
A_2	[−0.1, 0.1]
A_3	[−1.5, 1.5]

subspace are denoted as J_{ij}, those involving higher excited states as $J_{i\bar{j}}$, and mixed-state interactions as $J_{\bar{i}\bar{j}}$. This notation extends naturally to higher excitation levels; for instance, interactions involving the third excited state are marked with a double overline, such as $J_{\bar{\bar{i}}\bar{j}}$. In particular, qubit-qubit detunings are denoted with overlines when they correspond to transitions outside the computational subspace, e.g., $\Delta_{\bar{i}j}$ or $\Delta_{\bar{\bar{i}}\bar{j}}$, more details can be found in Ref. [40].

In this analysis, we assume $\Omega_2 \ll \Omega_1(\Omega_3)$, reflecting the fact that the target drive primarily serves to cancel classical crosstalk [27,54]. Under these conventions, the perturbative expressions to the first order in Ω for all relevant Pauli terms are given by

$$\alpha_{ZIX} = \frac{1}{2}\left[\Omega_1\cos\phi_1\left(\frac{J_{\bar{1}2}}{\Delta_{\bar{1}2}} - \frac{J_{12}}{\Delta_{12}} + \frac{J_{1\bar{3}}J_{\bar{3}2}}{\Delta_{13}\Delta_{\bar{3}2}} - \frac{J_{\bar{1}\bar{3}}J_{\bar{3}2}}{\Delta_{1\bar{2}}\Delta_{\bar{3}2}}\right) + \Omega_3\cos\phi_3\left(\frac{J_{1\bar{3}}J_{12}}{\Delta_{\bar{3}2}\Delta_{12}} - \frac{J_{\bar{1}\bar{3}}J_{\bar{1}2}}{\Delta_{\bar{3}2}\Delta_{\bar{1}2}}\right)\right] + \frac{\Omega_2}{4}\cos\phi_2\left[\left(\frac{J_{\bar{1}2}}{\Delta_{\bar{1}2}}\right)^2 + \left(\frac{J_{1\bar{2}}}{\Delta_{1\bar{2}}}\right)^2 - 2\frac{J_{12}J_{1\bar{2}}}{\Delta_{12}\Delta_{1\bar{2}}}\right] \tag{A3}$$

$$\alpha_{ZIY} = \frac{1}{2}\left[\Omega_1\sin\phi_1\left(\frac{J_{\bar{1}2}}{\Delta_{\bar{1}2}} - \frac{J_{12}}{\Delta_{12}} + \frac{J_{1\bar{3}}J_{\bar{3}2}}{\Delta_{13}\Delta_{\bar{3}2}} - \frac{J_{\bar{1}\bar{3}}J_{\bar{3}2}}{\Delta_{1\bar{2}}\Delta_{\bar{3}2}}\right) + \Omega_3\sin\phi_3\left(\frac{J_{1\bar{3}}J_{12}}{\Delta_{\bar{3}2}\Delta_{12}} - \frac{J_{\bar{1}\bar{3}}J_{\bar{1}2}}{\Delta_{\bar{3}2}\Delta_{\bar{1}2}}\right)\right] + \frac{\Omega_2}{4}\sin\phi_2\left[\left(\frac{J_{\bar{1}2}}{\Delta_{\bar{1}2}}\right)^2 + \left(\frac{J_{1\bar{2}}}{\Delta_{1\bar{2}}}\right)^2 - 2\frac{J_{12}J_{1\bar{2}}}{\Delta_{12}\Delta_{1\bar{2}}}\right] \tag{A4}$$

$$\alpha_{IZX} = \frac{1}{2}\left[\Omega_3\cos\phi_3\left(\frac{J_{\bar{3}2}}{\Delta_{\bar{3}2}} - \frac{J_{32}}{\Delta_{32}} + \frac{J_{1\bar{3}}J_{\bar{1}2}}{\Delta_{1\bar{2}}\Delta_{\bar{3}2}} - \frac{J_{\bar{1}\bar{3}}J_{\bar{1}2}}{\Delta_{\bar{1}2}\Delta_{\bar{3}2}}\right) + \Omega_1\cos\phi_1\left(\frac{J_{\bar{1}3}J_{32}}{\Delta_{\bar{1}2}\Delta_{32}} - \frac{J_{\bar{1}\bar{3}}J_{\bar{3}2}}{\Delta_{\bar{1}2}\Delta_{\bar{3}2}}\right)\right] + \frac{\Omega_2}{4}\cos\phi_2\left[\left(\frac{J_{\bar{3}2}}{\Delta_{\bar{3}2}}\right)^2 + \left(\frac{J_{3\bar{2}}}{\Delta_{3\bar{2}}}\right)^2 - 2\frac{J_{32}J_{3\bar{2}}}{\Delta_{32}\Delta_{3\bar{2}}}\right] \tag{A5}$$

$$\alpha_{IZY} = \frac{1}{2}\left[\Omega_3\sin\phi_3\left(\frac{J_{\bar{3}2}}{\Delta_{\bar{3}2}} - \frac{J_{32}}{\Delta_{32}} + \frac{J_{1\bar{3}}J_{\bar{1}2}}{\Delta_{1\bar{2}}\Delta_{\bar{3}2}} - \frac{J_{\bar{1}\bar{3}}J_{\bar{1}2}}{\Delta_{\bar{1}2}\Delta_{\bar{3}2}}\right) + \Omega_1\sin\phi_1\left(\frac{J_{\bar{1}3}J_{32}}{\Delta_{\bar{1}2}\Delta_{32}} - \frac{J_{\bar{1}\bar{3}}J_{\bar{3}2}}{\Delta_{\bar{1}2}\Delta_{\bar{3}2}}\right)\right] + \frac{\Omega_2}{4}\sin\phi_2\left[\left(\frac{J_{\bar{3}2}}{\Delta_{\bar{3}2}}\right)^2 + \left(\frac{J_{3\bar{2}}}{\Delta_{3\bar{2}}}\right)^2 - 2\frac{J_{32}J_{3\bar{2}}}{\Delta_{32}\Delta_{3\bar{2}}}\right] \tag{A6}$$

$$\alpha_{IIX} = \frac{1}{2}\left[\Omega_2\cos\phi_2 - \Omega_1\cos\phi_1\left(\frac{J_{\bar{1}2}}{\Delta_{\bar{1}2}} - \frac{J_{\bar{1}\bar{3}}J_{\bar{3}2}}{\Delta_{\bar{1}2}\Delta_{\bar{3}2}}\right) - \Omega_3\cos\phi_3\left(\frac{J_{\bar{3}2}}{\Delta_{\bar{3}2}} - \frac{J_{\bar{1}\bar{3}}J_{\bar{1}2}}{\Delta_{\bar{1}2}\Delta_{\bar{3}2}}\right)\right] \tag{A7}$$

$$\alpha_{IIY} = \frac{1}{2}\left[\Omega_2\sin\phi_2 - \Omega_1\sin\phi_1\left(\frac{J_{\bar{1}2}}{\Delta_{\bar{1}2}} - \frac{J_{\bar{1}\bar{3}}J_{\bar{3}2}}{\Delta_{\bar{1}2}\Delta_{\bar{3}2}}\right) - \Omega_3\sin\phi_3\left(\frac{J_{\bar{3}2}}{\Delta_{\bar{3}2}} - \frac{J_{\bar{1}\bar{3}}J_{\bar{1}2}}{\Delta_{\bar{1}2}\Delta_{\bar{3}2}}\right)\right] \tag{A8}$$

$$\alpha_{ZZX} = \frac{\Omega_1}{2}\cos\phi_1\left(\frac{J_{32}}{\Delta_{32}}\frac{J_{13}}{\Delta_{12}} - \frac{J_{32}}{\Delta_{32}}\frac{J_{\bar{1}\bar{3}}}{\Delta_{\bar{1}2}} - \frac{J_{\bar{3}2}}{\Delta_{\bar{3}2}}\frac{J_{1\bar{3}}}{\Delta_{12}} + \frac{J_{\bar{3}2}}{\Delta_{\bar{3}2}}\frac{J_{\bar{1}\bar{3}}}{\Delta_{\bar{1}2}}\right) + \frac{\Omega_3}{2}\cos\phi_3\left(\frac{J_{12}}{\Delta_{12}}\frac{J_{13}}{\Delta_{32}} - \frac{J_{12}}{\Delta_{12}}\frac{J_{1\bar{3}}}{\Delta_{\bar{3}2}} - \frac{J_{\bar{1}2}}{\Delta_{\bar{1}2}}\frac{J_{\bar{1}3}}{\Delta_{3\bar{2}}} + \frac{J_{\bar{1}2}}{\Delta_{\bar{1}2}}\frac{J_{\bar{1}\bar{3}}}{\Delta_{\bar{3}2}}\right) \tag{A9}$$

$$\alpha_{ZZY} = \frac{\Omega_1}{2}\sin\phi_1\left(\frac{J_{32}}{\Delta_{32}}\frac{J_{13}}{\Delta_{12}} - \frac{J_{32}}{\Delta_{32}}\frac{J_{\bar{1}\bar{3}}}{\Delta_{\bar{1}2}} - \frac{J_{\bar{3}2}}{\Delta_{\bar{3}2}}\frac{J_{1\bar{3}}}{\Delta_{12}} + \frac{J_{\bar{3}2}}{\Delta_{\bar{3}2}}\frac{J_{\bar{1}\bar{3}}}{\Delta_{\bar{1}2}}\right) + \frac{\Omega_3}{2}\sin\phi_3\left(\frac{J_{12}}{\Delta_{12}}\frac{J_{13}}{\Delta_{32}} - \frac{J_{12}}{\Delta_{12}}\frac{J_{1\bar{3}}}{\Delta_{\bar{3}2}} - \frac{J_{\bar{1}2}}{\Delta_{\bar{1}2}}\frac{J_{\bar{1}3}}{\Delta_{3\bar{2}}} + \frac{J_{\bar{1}2}}{\Delta_{\bar{1}2}}\frac{J_{\bar{1}\bar{3}}}{\Delta_{\bar{3}2}}\right). \tag{A10}$$

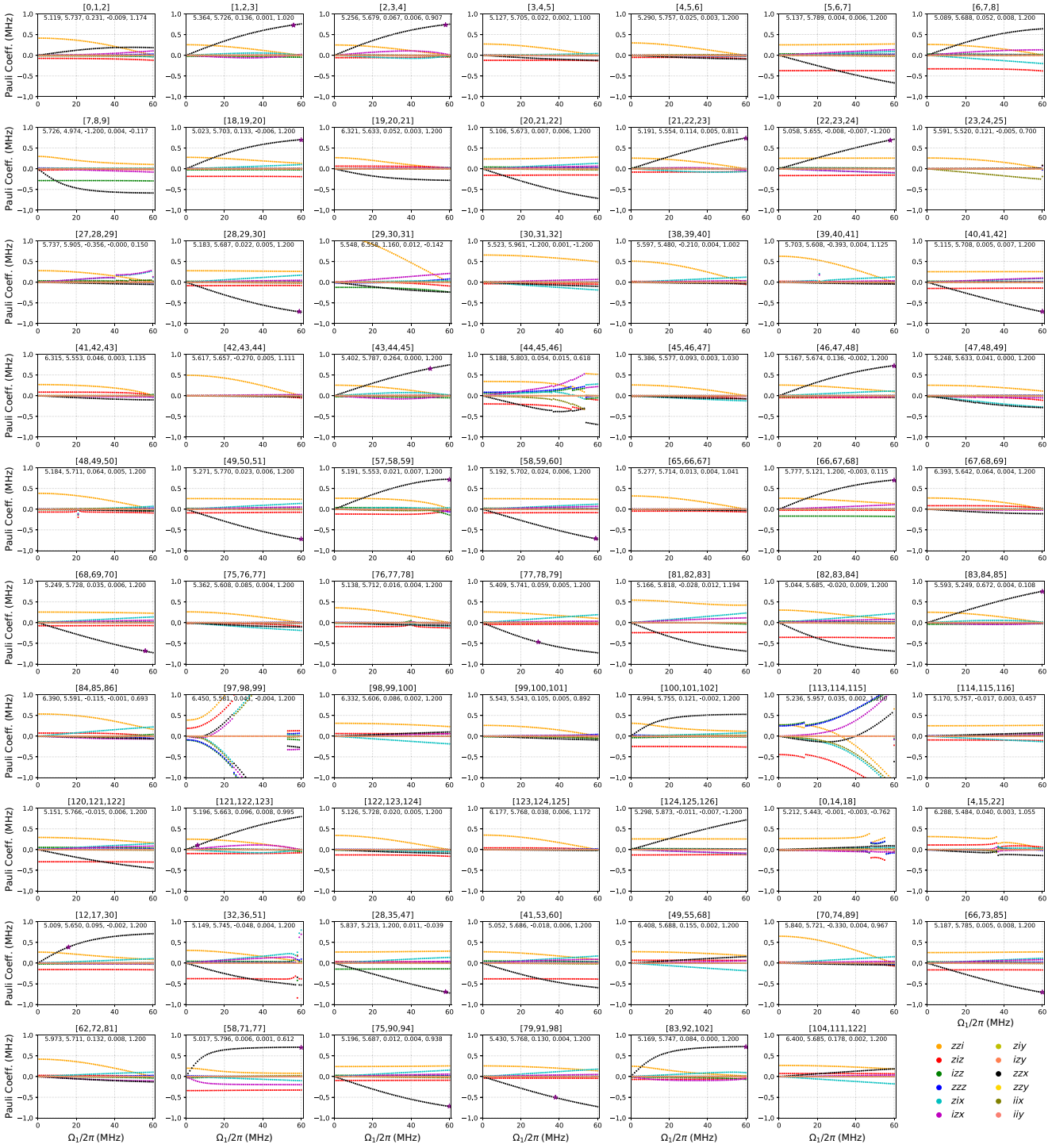

FIG. 8. Verification of Pauli coefficients for GHZ state generation using optimized parameters, with Q_1 and Q_3 serving as control qubits and Q_2 as the target qubit. The title of each panel indicates the labels of the evaluated qubits. The inset shows the optimized parameters in the form $[\omega_{c_{12}}, \omega_{c_{23}}, A_1, A_2, A_3]$, where $A_j = \Omega_j / \Omega$, and Ω is the drive amplitude plotted along the x axis. In selected panels where GHZ state fidelity exceeding 90%, the star marks the drive amplitude at which the GHZ state reaches its maximum fidelity.

Numerical simulations remain stable for maximum excitation numbers above four, as illustrated by unit cell 2 in the GHZ state implementation shown in Fig. 7.

APPENDIX B: ALGORITHMIC FRAMEWORK

This section describes the selection of initial tunable parameters for the optimization algorithm and the

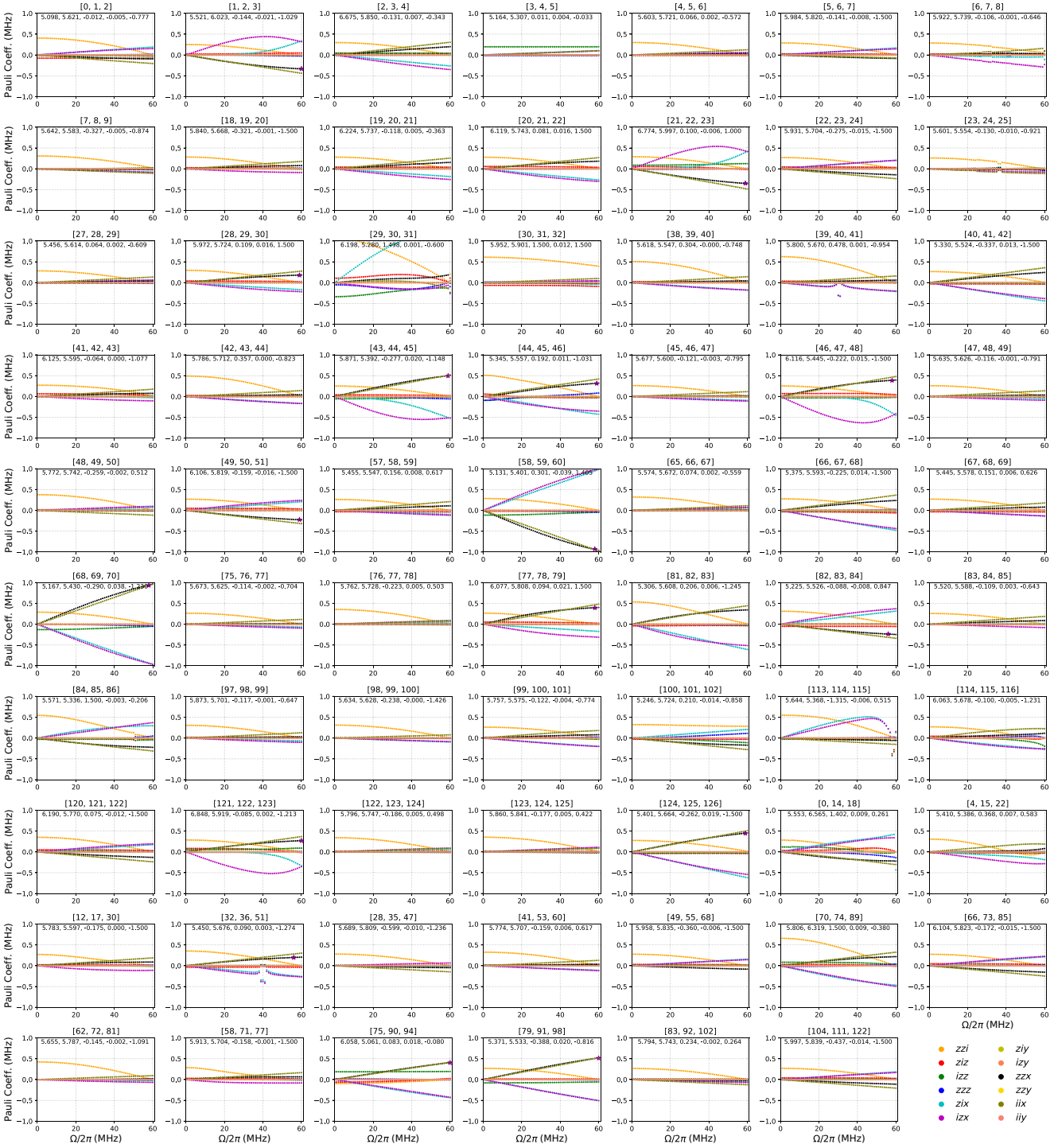

FIG. 9. Verification of Pauli coefficients for generating *i*Toffoli gate using optimized parameters, with Q_1 and Q_3 serving as control qubits and Q_2 as the target qubit. The title of each panel indicates the labels of the evaluated qubits. The inset shows the optimized parameters in the form $[\omega_{c_{12}}, \omega_{c_{23}}, A_1, A_2, A_3]$, where $\mathrm{A}_j = \Omega_j / \Omega$, and Ω is the drive amplitude plotted along the x-axis. In selected panel where *i*Toffoli gate fidelity exceeding 90%, the star marks the drive amplitude at which the *i*Toffoli gate reaches its maximum fidelity.

cost-function definition. Throughout the protocols for GHZ state preparation, *i*Toffoli (CCNOT), and CZZ gate implementations, we fix the target interaction strength as $\alpha_{ZZX}^{\mathrm{opt}} = 0.5$ MHz. Qubit Q_2 is consistently the target qubit for GHZ and *i*Toffoli gates, while for the CZZ gate, Q_1 acts as the measurement qubit, with Q_2 and Q_3 as data qubits.

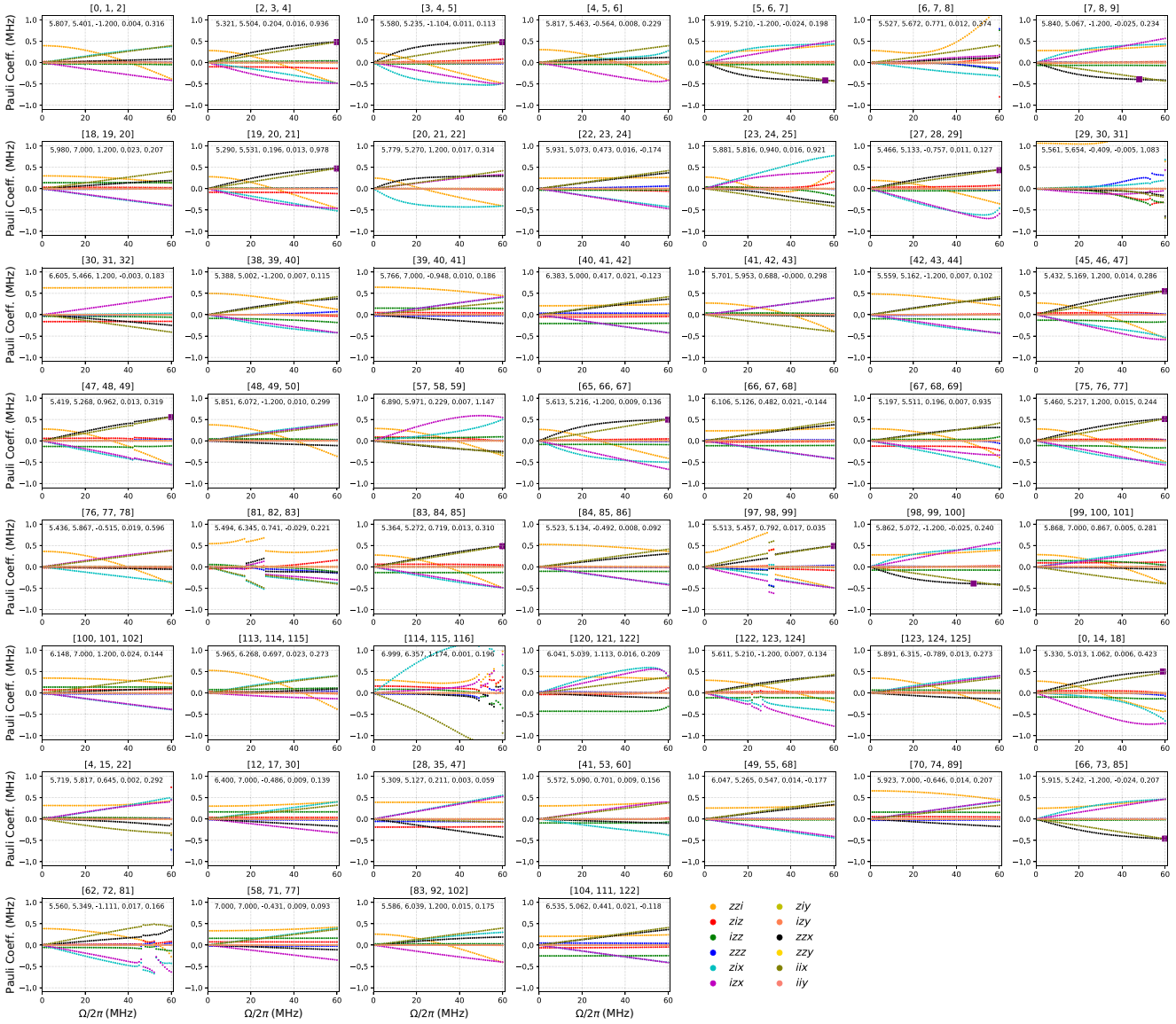

FIG. 10. Verification of Pauli coefficients for generating CCNOT gate using optimized parameters, with Q_1 and Q_3 serving as control qubits and Q_2 as the target qubit. The title of each panel indicates the labels of the evaluated qubits. The inset shows the optimized parameters in the form $[\omega_{c_{12}}, \omega_{c_{23}}, A_1, A_2, A_3]$, where $A_j = \Omega_j / \Omega$, and Ω is the drive amplitude plotted along the x-axis. In selected panel where CCNOT gate fidelity exceeding 90%, the square marks the drive amplitude at which the CCNOT gate reaches its maximum fidelity.

Given five control parameters, $\omega_{c_{12}}$, $\omega_{c_{23}}$, A_1, A_2, and A_3, the number of independent constraints does not exceed this count. For GHZ state generation, the protocol assumes $\alpha_{ZIX} \approx \alpha_{IZX} \approx -\alpha_{IIX}$ and enhances α_{ZZX} to $\alpha_{ZZX}^{\text{opt}}$, while suppressing undesired terms. For the iToffoli gate, symmetry conditions impose $\alpha_{IZX} \approx \alpha_{ZIX} \approx -\alpha_{ZZX} \approx \alpha_{IIX}$. The CCNOT gate requires $\alpha_{IZX} \approx \alpha_{ZIX} \approx \alpha_{ZZI} \approx -\alpha_{ZZX} \approx -\alpha_{IIX}$. For the CZZ gate, the key relation is $\alpha_{IZX} = -\alpha_{ZZX}$, with other terms suppressed.

Representative initial parameters satisfying these conditions for unit cells 2 ([1, 2, 3]) and 3 ([2, 3, 4]) are summarized in Table II.

The optimization algorithm is performed subject to the parameter constraints listed in Table III.

APPENDIX C: VALIDATION OF PAULI COEFFICIENTS

To confirm the effectiveness of the optimization procedure, we validate the reconstructed Pauli coefficients

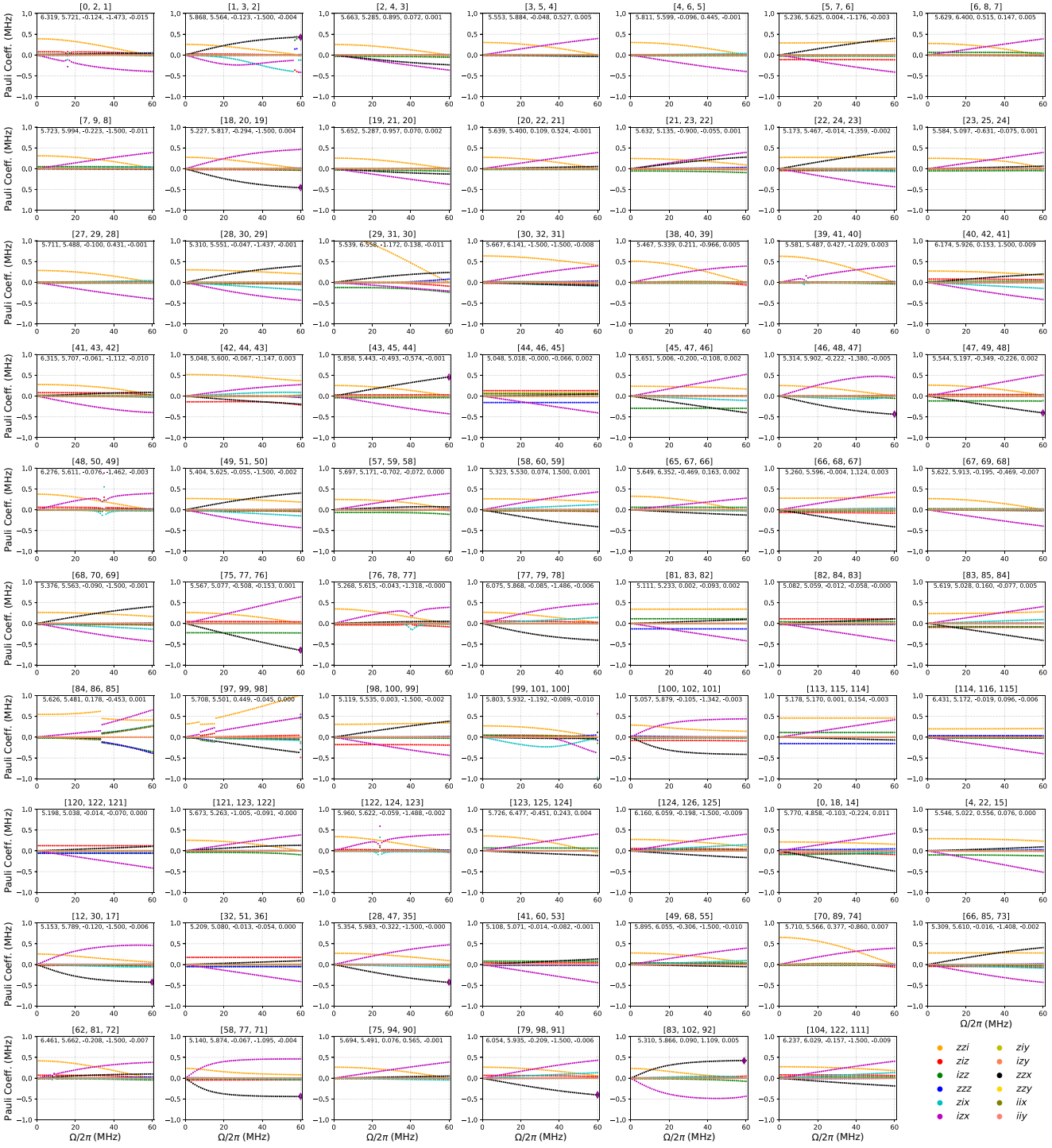

FIG. 11. Verification of Pauli coefficients for generating CZZ gate using optimized parameters, with Q_1 serving as measure qubits, Q_2 and Q_3 as the data qubit. The title of each panel indicates the labels of the evaluated qubits. The inset shows the optimized parameters in the form $[\omega_{c_{12}}, \omega_{c_{23}}, A_1, A_2, A_3]$, where $A_j = \Omega_j / \Omega$, and Ω is the drive amplitude plotted along the x-axis. In selected panel where CZZ gate fidelity exceeding 90%, the diamond marks the drive amplitude at which the CZZ gate reaches its maximum fidelity.

associated with both GHZ state generation and the *i*Toffoli gate implementation using our software CirQubit [48]. Figures 8 and 9 display the extracted coefficients obtained from the nonperturbative Hamiltonian reconstruction using the optimized parameters for the GHZ state and the *i*Toffoli gate, respectively.

[1] A. Kandala, K. X. Wei, S. Srinivasan, E. Magesan, S. Carnevale, G. A. Keefe, D. Klaus, O. Dial, and D. C. McKay, Demonstration of a high-fidelity CNOT gate for fixed-frequency transmons with engineered *ZZ* suppression, Phys. Rev. Lett. **127**, 130501 (2021).

[2] Y. Sung, L. Ding, J. Braumüller, A. Vepsäläinen, B. Kannan, M. Kjaergaard, A. Greene, G. O. Samach, C. McNally, D. Kim, A. Melville, B. M. Niedzielski, M. E. Schwartz, J. L. Yoder, T. P. Orlando, S. Gustavsson, and W. D. Oliver, Realization of high-fidelity *CZ* and *ZZ*-free iSWAP gates with a tunable coupler, Phys. Rev. X **11**, 021058 (2021).

[3] I. N. Moskalenko, I. A. Simakov, N. N. Abramov, A. A. Grigorev, D. O. Moskalev, A. A. Pishchimova, N. S. Smirnov, E. V. Zikiy, I. A. Rodionov, and I. S. Besedin, High fidelity two-qubit gates on fluxoniums using a tunable coupler, npj Quantum Inf. **8**, 130 (2022).

[4] H. Hahn, G. Zarantonello, M. Schulte, A. Bautista-Salvador, K. Hammerer, and C. Ospelkaus, Integrated $^{9}Be^{+}$ multi-qubit gate device for the ion-trap quantum computer, npj Quantum Inf. **5**, 70 (2019).

[5] C. D. Bruzewicz, R. McConnell, J. Stuart, J. M. Sage, and J. Chiaverini, Dual-species, multi-qubit logic primitives for Ca^{+}/Sr^{+} trapped-ion crystals, npj Quantum Inf. **5**, 102 (2019).

[6] N. Grzesiak, R. Blümel, K. Wright, K. M. Beck, N. C. Pisenti, M. Li, V. Chaplin, J. M. Amini, S. Debnath, J.-S. Chen, and Y. Nam, Efficient arbitrary simultaneously entangling gates on a trapped-ion quantum computer, Nat. Commun. **11**, 2963 (2020).

[7] R. Blümel, N. Grzesiak, N. Pisenti, K. Wright, and Y. Nam, Power-optimal, stabilized entangling gate between trapped-ion qubits, npj Quantum Inf. **7**, 147 (2021).

[8] H. Levine, A. Keesling, G. Semeghini, A. Omran, T. T. Wang, S. Ebadi, H. Bernien, M. Greiner, V. Vuletić, H. Pichler, and M. D. Lukin, Parallel implementation of high-fidelity multiqubit gates with neutral atoms, Phys. Rev. Lett. **123**, 170503 (2019).

[9] M. Khazali and K. Mølmer, Fast multiqubit gates by adiabatic evolution in interacting excited-state manifolds of Rydberg atoms and superconducting circuits, Phys. Rev. X **10**, 021054 (2020).

[10] S. J. Evered, D. Bluvstein, M. Kalinowski, S. Ebadi, T. Manovitz, H. Zhou, S. H. Li, A. A. Geim, T. T. Wang, N. Maskara, H. Levine, G. Semeghini, M. Greiner, V. Vuletić, and M. D. Lukin, High-fidelity parallel entangling gates on a neutral-atom quantum computer, Nature **622**, 268 (2023).

[11] A. Cao, W. J. Eckner, T. Lukin Yelin, A. W. Young, S. Jandura, L. Yan, K. Kim, G. Pupillo, J. Ye, N. Darkwah Oppong, and A. M. Kaufman, Multi-qubit gates and schrödinger cat states in an optical clock, Nature **634**, 315 (2024).

[12] Y. Kim, A. Morvan, L. B. Nguyen, R. K. Naik, C. Jünger, L. Chen, J. M. Kreikebaum, D. I. Santiago, and I. Siddiqi, High-fidelity three-qubit *i*Toffoli gate for fixed-frequency superconducting qubits, Nat. Phys. **18**, 783 (2022).

[13] T. Menke, W. P. Banner, T. R. Bergamaschi, A. Di Paolo, A. Vepsäläinen, S. J. Weber, R. Winik, A. Melville, B. M. Niedzielski, D. Rosenberg, K. Serniak, M. E. Schwartz, J. L. Yoder, A. Aspuru-Guzik, S. Gustavsson, J. A. Grover, C. F. Hirjibehedin, A. J. Kerman, and W. D. Oliver, Demonstration of tunable three-body interactions between superconducting qubits, Phys. Rev. Lett. **129**, 220501 (2022).

[14] C. W. Warren, J. Fernández-Pendás, S. Ahmed, T. Abad, A. Bengtsson, J. Biznárová, K. Debnath, X. Gu, C. Križan, A. Osman, A. Fadavi Roudsari, P. Delsing, G. Johansson, A. Frisk Kockum, G. Tancredi, and J. Bylander, Extensive characterization and implementation of a family of three-qubit gates at the coherence limit, npj Quantum Inf. **9**, 44 (2023).

[15] X. Xu, Manabputra, C. Vignes, M. H. Ansari, and J. M. Martinis, Lattice hamiltonians and stray interactions within quantum processors, Phys. Rev. Appl. **22**, 064030 (2024).

[16] Z. Chen, W. Liu, Y. Ma, W. Sun, R. Wang, H. Wang, H. Xu, G. Xue, H. Yan, Z. Yang, J. Ding, Y. Gao, F. Li, Y. Zhang, Z. Zhang, Y. Jin, H. Yu, J. Chen, and F. Yan, Efficient implementation of arbitrary two-qubit gates using unified control, Nat. Phys. **21**, 1489 (2025).

[17] A. Javadi-Abhari, S. Martiel, A. Seif, M. Takita, and K. X. Wei, Big cats: Entanglement in 120 qubits and beyond, ArXiv:2510.09520.

[18] M. T. P. Nguyen, M. Rimbach-Russ, L. M. K. Vandersypen, and S. Bosco, Single-step high-fidelity three-qubit gates by anisotropic chiral interactions, PRX Quantum **6**, 030326 (2025).

[19] X. Gu, J. Fernández-Pendás, P. Vikstål, T. Abad, C. Warren, A. Bengtsson, G. Tancredi, V. Shumeiko, J. Bylander, G. Johansson, and A. F. Kockum, Fast multiqubit gates through simultaneous two-qubit gates, PRX Quantum **2**, 040348 (2021).

[20] S. Tasler, J. Old, L. Heunisch, V. Feulner, T. Eckstein, M. Müller, and M. J. Hartmann, Optimizing superconducting three-qubit gates for surface-code error correction, ArXiv:2506.09028.

[21] J. Old, S. Tasler, M. J. Hartmann, and M. Müller, Fault-tolerant stabilizer measurements in surface codes with three-qubit gates, Phys. Rev. Lett. **135**, 240601 (2025).

[22] T. Itoko, M. Malekakhlagh, N. Kanazawa, and M. Takita, Three-qubit parity gate via simultaneous cross-resonance drives, Phys. Rev. Appl. **21**, 034018 (2024).

[23] C. Rigetti and M. Devoret, Fully microwave-tunable universal gates in superconducting qubits with linear couplings and fixed transition frequencies, Phys. Rev. B **81**, 134507 (2010).

[24] J. M. Chow, A. D. Córcoles, J. M. Gambetta, C. Rigetti, B. R. Johnson, J. A. Smolin, J. R. Rozen, G. A. Keefe, M. B. Rothwell, M. B. Ketchen, and M. Steffen, Simple all-microwave entangling gate for fixed-frequency superconducting qubits, Phys. Rev. Lett. **107**, 080502 (2011).

[25] J. M. Chow, J. M. Gambetta, A. D. Córcoles, S. T. Merkel, J. A. Smolin, C. Rigetti, S. Poletto, G. A. Keefe, M. B. Rothwell, J. R. Rozen, M. B. Ketchen, and M. Steffen, Universal quantum gate set approaching fault-tolerant thresholds with superconducting qubits, Phys. Rev. Lett. **109**, 060501 (2012).

[26] A. D. Córcoles, J. M. Gambetta, J. M. Chow, J. A. Smolin, M. Ware, J. Strand, B. L. T. Plourde, and M. Steffen, Process verification of two-qubit quantum gates by randomized benchmarking, Phys. Rev. A **87**, 030301(R) (2013).

[27] S. Sheldon, E. Magesan, J. M. Chow, and J. M. Gambetta, Procedure for systematically tuning up cross-talk in the cross-resonance gate, Phys. Rev. A **93**, 060302(R) (2016).
[28] E. Magesan and J. M. Gambetta, Effective hamiltonian models of the cross-resonance gate, Phys. Rev. A **101**, 052308 (2020).
[29] M. Ansari and X. Xu, Three-qubit gate and method for its realization, European Patent EP4571596, https://register.epo.org/application?number=EP23215766&tab=main (Issued on June 18, 2025).
[30] M. Hillery, V. Bužek, and A. Berthiaume, Quantum secret sharing, Phys. Rev. A **59**, 1829 (1999).
[31] H. Buhrman, R. Cleve, S. Massar, and R. de Wolf, Nonlocality and communication complexity, Rev. Mod. Phys. **82**, 665 (2010).
[32] D. P. DiVincenzo and P. W. Shor, Fault-tolerant error correction with efficient quantum codes, Phys. Rev. Lett. **77**, 3260 (1996).
[33] J. Preskill, Reliable quantum computers, Proc. R. Soc. Lond. Ser. A **454**, 385 (1998).
[34] S. Bose, V. Vedral, and P. L. Knight, Multiparticle generalization of entanglement swapping, Phys. Rev. A **57**, 822 (1998).
[35] C.-P. Yang, S.-I. Chu, and S. Han, Efficient many-party controlled teleportation of multiqubit quantum information via entanglement, Phys. Rev. A **70**, 022329 (2004).
[36] J. Pazem and M. H. Ansari, Error mitigation in brainbox quantum autoencoders, Sci. Rep. **15**, 2257 (2025).
[37] M. A. Nielsen and I. Chuang, *Quantum Computation and Quantum Information: 10th Anniversary Edition* (Cambridge University Press, Cambridge, 2010).
[38] V. V. Shende and I. L. Markov, On the CNOT-cost of Toffoli gates, Quantum Inf. Comput. **9**, 461 (2009).
[39] Y.-W. Cho, Y. Kim, Y.-H. Choi, Y.-S. Kim, S.-W. Han, S.-Y. Lee, S. Moon, and Y.-H. Kim, Emergence of the geometric phase from quantum measurement back-action, Nat. Phys. **15**, 665 (2019).
[40] X. Xu, K. Kaur, C. Vignes, M. H. Ansari, and J. M. Martinis, Surface-code hardware Hamiltonian, ArXiv:2507.06201.
[41] M. H. Ansari, Superconducting qubits beyond the dispersive regime, Phys. Rev. B **100**, 024509 (2019).
[42] S. Bravyi, D. P. DiVincenzo, and D. Loss, Schrieffer–Wolff transformation for quantum many-body systems, Ann. Phys. (N. Y.) **326**, 2793 (2011).
[43] M. Serbyn, Z. Papić, and D. A. Abanin, Local conservation laws and the structure of the many-body localized states, Phys. Rev. Lett. **111**, 127201 (2013).
[44] M. Schreiber, S. S. Hodgman, P. Bordia, H. P. Lüschen, M. H. Fischer, R. Vosk, E. Altman, U. Schneider, and I. Bloch, Observation of many-body localization of interacting fermions in a quasirandom optical lattice, Science **349**, 842 (2015).
[45] C. Berke, E. Varvelis, S. Trebst, A. Altland, and D. P. DiVincenzo, Transmon platform for quantum computing challenged by chaotic fluctuations, Nat. Commun. **13**, 2495 (2022).
[46] T. McBroom-Carroll, A. Schlabes, X. Xu, J. Ku, B. Cole, S. Indrajeet, M. D. LaHaye, M. H. Ansari, and B. L. T. Plourde, Entangling interactions between artificial atoms mediated by a multimode left-handed superconducting ring resonator, PRX Quantum **5**, 020325 (2024).
[47] L. S. Cederbaum, J. Schirmer, and H. D. Meyer, Block diagonalisation of hermitian matrices, J. Phys. A: Math. Gen. **22**, 2427 (1989).
[48] Cirqubit, Software suite for simulating superconducting qubits, https://cirqubit.com (2024).
[49] F. Motzoi, J. M. Gambetta, S. T. Merkel, and F. K. Wilhelm, Optimal control methods for rapidly time-varying hamiltonians, Phys. Rev. A **84**, 022307 (2011).
[50] T. Caneva, T. Calarco, and S. Montangero, Chopped random-basis quantum optimization, Phys. Rev. A **84**, 022326 (2011).
[51] S. Machnes, E. Assémat, D. Tannor, and F. K. Wilhelm, Tunable, flexible, and efficient optimization of control pulses for practical qubits, Phys. Rev. Lett. **120**, 150401 (2018).
[52] X. Xu and M. Ansari, Parasitic-free gate: An error-protected cross-resonance switch in weakly tunable architectures, Phys. Rev. Appl. **19**, 024057 (2023).
[53] X. Xu and M. H. Ansari, *zz* freedom in two-qubit gates, Phys. Rev. Appl. **15**, 064074 (2021).
[54] J. Ku, X. Xu, M. Brink, D. C. McKay, J. B. Hertzberg, M. H. Ansari, and B. L. T. Plourde, Suppression of unwanted *ZZ* interactions in a hybrid two-qubit system, Phys. Rev. Lett. **125**, 200504 (2020).
[55] P. Zhao, P. Xu, D. Lan, J. Chu, X. Tan, H. Yu, and Y. Yu, High-contrast *ZZ* interaction using superconducting qubits with opposite-sign anharmonicity, Phys. Rev. Lett. **125**, 200503 (2020).
[56] Z. Ni, S. Li, L. Zhang, J. Chu, J. Niu, T. Yan, X. Deng, L. Hu, J. Li, Y. Zhong, S. Liu, F. Yan, Y. Xu, and D. Yu, Scalable method for eliminating residual *ZZ* interaction between superconducting qubits, Phys. Rev. Lett. **129**, 040502 (2022).
[57] M. Ansari and X. Xu, Method of operating a circuit with a first and a second qubit, European Patent EP4205044, https://register.epo.org/application?number=EP21763382&tab=main (issued on May 7, 2023).
[58] M. Ansari and X. Xu, Circuit with coupled qubits with different anharmonic energy spectrum, Germany Patent DE102020201688B3, https://patents.google.com/patent/DE102020201688B3/en?inventor=xuexin+xu&oq=xuexin+xu (issued on July 29, 2021).
[59] M. Mohseni *et al.*, How to build a quantum supercomputer: Scaling from hundreds to millions of qubits, ArXiv:2411.10406.
[60] X. Croot *et al.*, Enabling technologies for scalable superconducting quantum computing, ArXiv:2512.15001.